

**Understanding the Reaction Energetics of Oxygen-evolving Electrocatalysts**

**Keywords:** transition metal doped ruthenium oxides, oxygen evolution reaction.

**Authors:** Ziqing Lin<sup>1</sup>, Payal Chaudhary<sup>2</sup>, S. Avery Vigil<sup>1</sup>, Matteo Fratarcangeli<sup>1</sup>, Conner J. Soderstedt<sup>1</sup>, Vitaly Alexandrov<sup>2</sup>, Ivan A. Moreno-Hernandez<sup>1,3\*</sup>

**Affiliations:**

<sup>1</sup>Department of Chemistry, Duke University; Durham, North Carolina 27708, United States

<sup>2</sup>Department of Chemical and Biomolecular Engineering, University of Nebraska-Lincoln; Lincoln, Nebraska 68588, United States

<sup>3</sup>Lead contact

**Correspondence:** [ivan.moreno-hernandez@duke.edu](mailto:ivan.moreno-hernandez@duke.edu)

## **Supplementary Results and Discussion**

### *X-ray photoelectron spectroscopy*

Supplementary Fig. 18 shows the X-ray photoelectron spectroscopy (XPS) analysis of M-RuO<sub>x</sub>. XPS confirmed the inclusion of V, Cr, Mn, Fe, Ni and Co in M-RuO<sub>x</sub>, and indicated that Ru was present in the Ru (IV) oxidation state for both RuO<sub>2</sub> and M-RuO<sub>x</sub> (Supplementary Fig. 18). Compared to RuO<sub>2</sub>, the Ru 3d binding energy exhibited a positive shift in most of the M-RuO<sub>x</sub> except for a negative shift from 284.241 eV to 284.202 eV in V-RuO<sub>x</sub> (Supplementary Table 13, Supplementary Fig. 18i). The lattice oxygen binding energy for M-RuO<sub>x</sub> exhibited both positive and negative shifts (Supplementary Table 13, Supplementary Fig. 18j).

### *Non-rutile phase analysis*

The effect of 2 M HCl treatment in decreasing the concentration of non-rutile phases was confirmed with X-ray diffraction for Co-RuO<sub>x</sub> and Ni-RuO<sub>x</sub>, which exhibited contributions from Co<sub>3</sub>O<sub>4</sub> and NiO, respectively. Acid treatment was found to decrease the amount of Co<sub>3</sub>O<sub>4</sub> from 11.34 wt% to 2.12 wt%, and NiO from 32.71 wt% to 8.94 wt%, based on Rietveld Analysis (Supplementary Fig. 3). Size analysis from Rietveld fitting indicates that Co<sub>3</sub>O<sub>4</sub> and NiO contributed less than 0.02 % to the surface area of the acid treated samples. Electrochemical activity studies indicate that Co<sub>3</sub>O<sub>4</sub> and NiO exhibit minimal activity towards oxygen evolution compared to RuO<sub>2</sub> in 1.0 M perchloric acid (Supplementary Fig. 3). Thus, it is expected that the remaining non-rutile phases in the M-RuO<sub>x</sub> samples exhibit minimal contributions to electroadsorption analysis and electrochemical activity studies for the conditions presented herein.

Recent studies have showing that ruthenium oxide/metal oxide interfaces can exhibit substantial improvements in catalytic activity.<sup>1,4</sup> Nanocrystals of Co-RuO<sub>x</sub> were acid treated in 2 M HCl for different durations prior to electrochemical operation to determine potential catalytic enhancement from RuO<sub>2</sub>/Co<sub>3</sub>O<sub>4</sub> interfaces. X-ray diffraction Rietveld analysis indicated that as-synthesized Co-RuO<sub>x</sub> consisted of 11.34 wt% Co<sub>3</sub>O<sub>4</sub>. The Co<sub>3</sub>O<sub>4</sub> crystals exhibited larger crystalline sizes, with an expected 8.03 % surface area contribution for the sample. Treatment with 2 M HCl at 90 °C resulted in a decrease of the expected surface contribution, with 1 hour and 4 hours of treatment resulted in 0.34 % and 0.28 % surface area contributions from Co<sub>3</sub>O<sub>4</sub>. The Co-RuO<sub>x</sub> exhibited a slight decrease in activity at 10 mA cm<sup>-2</sup> from no acid treatment to 4 hours of acid treatment. Control studies with Co<sub>3</sub>O<sub>4</sub> indicate minimal activity towards the OER compared to Co-RuO<sub>x</sub>. The RuO<sub>2</sub> nanocrystals exhibited higher catalytic activity than Co-RuO<sub>x</sub> after 1 hour of acid treatment. Overall, these results suggest that RuO<sub>2</sub>/Co<sub>3</sub>O<sub>4</sub> interfaces did not substantially contribute to catalytic activity or electrochemically active surface area for the nanocrystals synthesized in this study.

### *Electrochemical characterization*

Extended cyclic voltammetry was collected on RuO<sub>2</sub>, V-RuO<sub>x</sub>, and Mn-RuO<sub>x</sub> to determine the influence of electrochemical cycling on electroadsorption features and electrochemical activity (Supplementary Fig. 17). In general, electroadsorption data exhibits minor differences in redox features from 3 to 100 cycles, with most of the differences observed during the first two cyclic voltammograms. The slight differences observed for \*OH-\*O-\*OOH binding energies between cyclic voltammograms followed the energy scaling relations determined for M-RuO<sub>x</sub> nanocrystals after 3 cyclic voltammograms (Supplementary Fig. 17j). Mn-RuO<sub>x</sub> exhibited stable electrochemical activity during cycling, whereas RuO<sub>2</sub> and V-RuO<sub>x</sub> exhibited a gradual decrease in electrochemical activity. However, prior studies have indicated that electrochemical instability on glassy carbon electrodes could be attributed to the gradual formation of an insulating oxide on the glassy carbon.<sup>5</sup>

## **Supplementary Methods**

### **Materials**

All chemicals were used as received, including ruthenium (III) chloride hydrate ( $\text{RuCl}_3 \cdot x \text{H}_2\text{O}$ , Sigma-Aldrich, 99.98%), sodium chloride ( $\text{NaCl}$ , Thermo Scientific, 99.0%), sodium sulfate ( $\text{Na}_2\text{SO}_4$ , Thermo Scientific, 99%), Nafion (Thermo Fisher Scientific, 5% w/w in water and 1-propanol), 2-propanol (IPA, Sigma-Aldrich, 99.9% HPLC grade), 2 M hydrochloric acid ( $\text{HCl}$ , Supelco), iron(III) chloride hexahydrate ( $\text{FeCl}_3 \cdot 6 \text{H}_2\text{O}$ , Sigma-Aldrich, > 98%), nickel(II) chloride hexahydrate ( $\text{NiCl}_2 \cdot 6 \text{H}_2\text{O}$ , Alfa Aesar, 99.9995%), vanadium(IV) oxide ( $\text{V}_2\text{O}_5$ , Thermo Scientific, 99%), cobalt(II) chloride hexahydrate ( $\text{CoCl}_2 \cdot 6 \text{H}_2\text{O}$ , Thermo Scientific, 99.998%), chromium(III) chloride hexahydrate ( $\text{CrCl}_3 \cdot 6 \text{H}_2\text{O}$ , Beantown Chemical, 99.5%), copper(II) chloride dihydrate ( $\text{CuCl}_2 \cdot 2 \text{H}_2\text{O}$ , ACS, 99 + %), manganese(II) chloride tetrahydrate ( $\text{MnCl}_2 \cdot 4 \text{H}_2\text{O}$ , Fisher Scientific, 98-101%), and zinc(II) chloride hydrate ( $\text{ZnCl}_2 \cdot \text{H}_2\text{O}$ , Invitrogen, 99.99%), ruthenium(IV) oxide ( $\text{RuO}_2$ , Sigma-Aldrich, 99.9% trace metal basis), nickel(II) oxide ( $\text{NiO}$ , Thermo Scientific, 99% metals basis), and cobalt(II, III) oxide (Sigma-Aldrich, 99.5% trace metals basis). Ultra-high purity water was obtained at 18.2 M $\Omega$  purity from a Millipore Direct-Q® 3 UV system.

### **Raman spectroscopy**

Raman spectroscopy was performed using a Horiba Jobin Yvon LabRam ARAMIS model located at the Shared Materials Instrumentation Facility at Duke University. Raman spectra were collected using a 633 nm wavelength laser, 1200 grooves  $\text{mm}^{-1}$  grating size, and a 50x working objective. The spectra range was collected from 100 to 1000  $\text{cm}^{-1}$  with an acquisition time of 10 seconds with 50 accumulations. Raman samples were prepared by pressing the dry nano-powder onto a small piece of carbon tape that was adhered to the top of an aluminum SEM stub.

### **Powder X-ray Diffraction**

Powder X-ray Diffraction (XRD) was conducted using an Anton Paar XRDynamic 500 diffractometer with a Pixos 2000 1D detector located at the Shared Materials Instrumentation Facility at Duke University. The X-ray source equipped was a Primus 3000  $\text{Cu } k_\alpha$  with 40kV voltage and 50mA current. The XRD data was collected from 10° to 80° with a Bragg-Brentano geometry and a 0.01° step size. Integration time varied from 80 to 130 seconds. To prepare XRD samples, nano-powder was drop-cast onto a glass slide which was then placed on a stainless-steel sample holder. The lattice parameters were calculated using the Rietveld refinement tool in CrystalDiffract software with a database  $\text{RuO}_2$  crystal structure as reference (ICSD-56007). The d-spacing was calculated using the following:

$$\frac{1}{d^2} = \frac{h^2 + k^2}{a^2} + \frac{l^2}{c^2} \quad (\text{Eq. S1})$$

The size analysis of non-rutile phases was performed using the Anton Paar XRDanalysis software.

### **TEM grid preparation**

To prepare well-dispersed nanocrystals for electron microscopy characterization, size-selective centrifugation was performed for each sample. A small amount of dry nano-powder was dispersed in 1 mL of water in a microcentrifuge tube, then centrifuged at 2000-5000 rpm for 1-4 minutes. The top 500-800  $\mu\text{L}$  of each supernatant was carefully transferred to a new microcentrifuge tube and diluted to 1 mL. This process was repeated as needed until the remaining suspension was a light grey color. After size selection, 5  $\mu\text{L}$  of each sample was drop-cast onto a copper TEM grid (Carbon film, 400 mesh copper grid from EMS) and dried under vacuum.

### **Transmission Electron Microscopy**

Transmission electron microscopy (TEM) characterization was performed using a FEI Tecnai G<sup>2</sup> Twin transmission electron microscope located at the Shared Materials Instrumentation Facility at Duke University with a Gatan OneView camera and a LaB<sub>6</sub> thermionic electron source. The pixel resolution of the images was 4k (4096 × 4096), which were all collected using an accelerating voltage of 200 kV and a spot size of 3. TEM images analysis and image changes, including cropping, recoloring, and rotation, were all performed using Gatan digital micrograph software (GMS). Selected area electron diffraction (SAED) patterns were collected using the diffraction mode of the TEM with the selected area electron diffraction aperture inserted. Rings observed between 3.5 nm<sup>-1</sup> and 3.8 nm<sup>-1</sup> in selected area electron diffraction patterns are associated with the Tecnai microscope utilized to collect the data, as has been previously observed with this microscope.<sup>1-3</sup>

### **X-ray Photoelectron Spectroscopy**

X-ray photoelectron spectroscopy was performed for all samples using a Thermo Scientific Nexsa G2 model located at the Shared Materials Instrumentation Facility at Duke University. The X-ray source equipped was a monochromated, micro-focused, low-power Al K $\alpha$  type, with a spot size set to 400  $\mu$ m. All survey scans were collected with 1 scan, 20 ms dwell time, 1 eV step size and 200 eV pass energy. For the survey scan, data was collected from -10 to 1200 eV. All the region scans were collected with 0.1 eV step size, 20 eV pass energy, 5 scans and 50 ms dwell time. For C 1s and Ru 3d region scan, the range was collected between 270-300 eV. For O 1s and V 2p region scan, the data was collected between 520-550 eV. The region scan for Fe 2p was collected between 702-720 eV. The region scan for Mn 2p was collected between 635-660 eV.

The samples were prepared by mixing dry powder with IPA and drop-casting onto a sliced n-type silicon (100) wafer. All XPS spectra binding energies were calibrated to the C 1s signal for adventitious carbon set to 248.8 eV. All the XPS fitting was conducted using CASA XPS software. The fit for Ru 3d /C 1s and O 1s region scan was performed following the anhydrous form of RuO<sub>2</sub> reported by Morgan et al. with a few modifications.<sup>6</sup> The line shape used for fitting each peak of Ru 3d was LF(0.25,1,45,280). The separation between Ru 3d<sub>5/2</sub> and Ru 3d<sub>3/2</sub> was restricted to 4.17 eV consistent with the literature.<sup>6</sup> C 1s fit was performed with a line shape of GL(30). The line shape used for fitting O 1s and O 1s satellite peak was LF(0.25,1,45,280). The FWHM ratio of O 1s satellite peak and O 1s main peak was constrained to be 1.6:1. The separation between O 1s and its satellite peak was restricted to 1.6 eV. The Mn 2p and Fe 2p region scans were fit following previously reported procedures.<sup>7</sup>

### **Scanning electron microscopy**

Scanning electron microscopy with energy dispersive X-ray spectroscopy characterization (SEM-EDS) was performed using an Apreo S model by ThermoFisher Scientific located at the Shared Materials Instrumentation Facility at Duke University. The EDS data was collected using an accelerating voltage of 20kV and an emission current of 0.8 nA with 100  $\mu$ s dwell time.

### **Scanning transmission electron microscopy**

Scanning transmission electron microscopy with energy dispersive X-ray spectroscopy characterization (STEM-EDS) was performed on Mn-RuO<sub>x</sub> using an aberration-corrected ThermoFisher Titan 80-300 microscope at the Analytical Instrumentation Facility located at North Carolina State University. For all measurements, an FEI double tilt holder with a molybdenum retention clip was employed. The STEM-EDS data was collected using FEI's Super-X Quad detector with a solid angle of 0.7 steradians. The accelerating voltage used for STEM-EDS was 200kV and prior to data collection a screen current was set to 200 pA. The frame time used was 622 ms and the dwell time used was 10  $\mu$ s. Additional STEM-EDS was performed on the rest of M-RuO<sub>x</sub> using a 200kV FEG (field emission gun) Thermo Fisher Talos F200X microscope located at the Analytical Instrumentation Facility located at North Carolina State University. For all measurements, gold grids (200-mesh, Electron Microscopy Sciences, catalog number: CF200-AU) and a

double-tilt holder with a Mo retention clip were employed. The STEM-EDS maps were collected between 300 to 1000 frames with screen current between 200 and 1500 pA and a dwell time of 10  $\mu$ s.

### Electrochemical data analysis

The series resistance was calculated from EIS from the high-frequency datapoint with the lowest real resistance. The electrochemistry data was corrected with 85% of the measured series resistance. The double-layer capacitance ( $C_{DL}$ ) was calculated in a low-potential region without electroadsorption using the following equation:

$$C_{DL} = \frac{I_{cap}}{v} \quad (\text{Eq. S2})$$

where  $v$  is the scan rate and  $I_{cap}$  is the capacitive current, which can be calculated using Eq. S3 with the resistance-corrected forward current ( $I_f$ ) and backward current ( $I_b$ ).<sup>8</sup>

$$I_{cap} = \frac{I_f - I_b}{2} \quad (\text{Eq. S3})$$

The roughness factor ( $R_f$ ) was calculated with Eq. S4:<sup>8</sup>

$$R_f = \frac{C_{DL}}{C_s A} \quad (\text{Eq. S4})$$

where  $A$  represents a geometric electrode area of 0.196  $\text{cm}^2$  and  $C_s$  represents a specific capacitance of 0.04  $\text{mF cm}^{-2}$ .<sup>8</sup> The roughness factor (RF) corresponds to the electrochemically active surface area in  $\text{cm}^2$  divided by the area of the rotating disk electrode (.196  $\text{cm}^2$ ). The ECSA-normalized current density ( $J_{ox}$ ) can be calculated with Eq S5:

$$J_{ox} = \frac{I}{AR_f} = \frac{J}{R_f} \quad (\text{Eq. S5})$$

Where  $J$  represents the experimentally measured geometric current density. The Tafel plot for each sample was obtained by fitting the exponential catalytic current from the slow scan CV within a given current density range. The average current density was extracted from the observed resistance-corrected forward and backward current density using the following equation:

$$J_{avg} = \frac{(J_f + J_b)}{2} \quad (\text{Eq. S6})$$

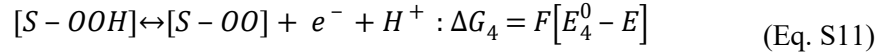
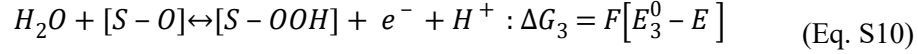
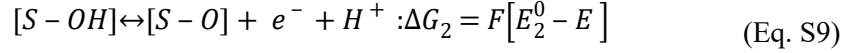
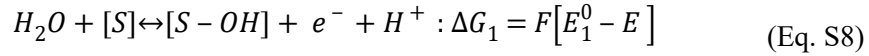
Where  $J_{avg}$  represents the average current density,  $J_f$  represents the observed forward current density, and  $J_b$  represents the observed backward current density. Then, using the Tafel equation (Eq. S7), the Tafel slope can be obtained.

$$\eta = S * \log_{10}\left(\frac{J_{avg}}{J_0}\right) \quad (\text{Eq. S7})$$

where  $\eta$  is the overpotential,  $S$  represents the Tafel slope, and  $J_0$  is the exchange current density.

### Oxygen Evolution Reaction Models

The five-step oxygen evolution reaction mechanism in acid was used for analysis, with the following elemental steps:



$$\Delta G_1^0 + \Delta G_2^0 + \Delta G_3^0 + \Delta G_4^0 + \Delta G_5^0 = 4.916 \text{ eV} \quad (\text{Eq. S13})$$

Where the empty active site is represented by S and \*OH, \*O, and \*OOH intermediates correspond to S-OH, S-O, and S-OOH, respectively,  $\Delta G_i$  indicates the reaction Gibbs free energy,  $E_i^0$  is the standard potential, and  $E$  is the applied potential vs. the RHE. Note that the reactions have been reversed so that the forward step corresponds to oxidation.

### Microkinetic simulation

A microkinetic OER model was built based on following reaction kinetics:

$$k_{fi} = k_0 e^{\frac{\alpha F}{RT} [E - E_i^0]} \quad (\text{Eq. S14})$$

$$k_{bi} = k_0 e^{\left[ -\frac{(1-\alpha)F}{RT} [E - E_i^0] \right]} \quad (\text{Eq. S15})$$

$$k_{f5} = k_0 \quad (\text{Eq. S16})$$

$$k_{b5} = k_0 e^{\left( \frac{\Delta G_5^0}{RT} \right)} \quad (\text{Eq. S17})$$

where  $\alpha$  represents the charge transfer coefficient for the forward reactions,  $E_i^0$  corresponds to the electrochemical potential of each elementary reaction step,  $k_0$  corresponds to the reaction rate constant which was set to  $10^3 \text{ s}^{-1}$ ,  $\Delta G_5^0$  is the Gibbs free energy for \*OO desorption to form  $O_2$ , R is the ideal gas constant, T is the temperature, F is Faraday's constant, and E is the applied voltage vs. the RHE.

The following rate laws were used to describe each elementary reaction step of the OER:

$$v_{f1} = k_{f1}[S][H_2O] \quad (\text{Eq. S18})$$

$$v_{b1} = k_{b1}[S - OH][H^+] \quad (\text{Eq. S19})$$

$$v_{f2} = k_{f2}[S - OH] \quad (\text{Eq. S20})$$

$$v_{b2} = k_{b2}[S - O][H^+] \quad (\text{Eq. S21})$$

$$v_{f3} = k_{f3}[S - O][H_2O] \quad (\text{Eq. S22})$$

$$v_{b3} = k_{b3}[S - OOH][H^+] \quad (\text{Eq. S23})$$

$$v_{f4} = k_{f4}[S - OOH] \quad (\text{Eq. S24})$$

$$v_{b4} = k_{b4}[S - OO][H^+] \quad (\text{Eq. S25})$$

$$v_{f5} = k_{f5}[S - OO] \quad (\text{Eq. S26})$$

$$v_{b5} = k_{b5}[S][O_2] \quad (\text{Eq. S27})$$

Where  $v_{fi}$  and  $v_{bi}$  correspond to the reaction velocities for each elementary reaction step. The overall change in surface coverage over time is the following:

$$\frac{\partial[S]}{\partial t} = -(v_{f1} - v_{b1}) + (v_{f5} - v_{b5}) \quad (\text{Eq. S28})$$

$$\frac{\partial[S - OH]}{\partial t} = (v_{f1} - v_{b1}) - (v_{f2} - v_{b2}) \quad (\text{Eq. S29})$$

$$\frac{\partial[S - O]}{\partial t} = (v_{f2} - v_{b2}) - (v_{f3} - v_{b3}) \quad (\text{Eq. S30})$$

$$\frac{\partial[S - OOH]}{\partial t} = (v_{f3} - v_{b3}) - (v_{f4} - v_{b4}) \quad (\text{Eq. S31})$$

$$\frac{\partial[S - OO]}{\partial t} = (v_{f4} - v_{b4}) - (v_{f5} - v_{b5}) \quad (\text{Eq. S32})$$

$$\frac{\partial[e^-]}{\partial t} = (v_{f1} - v_{b1}) + (v_{f2} - v_{b2}) + (v_{f3} - v_{b3}) + (v_{f4} - v_{b4}) \quad (\text{Eq. S33})$$

From the rate laws, the total number of electrons transferred versus time,  $e(t)$ , can be determined by solving the corresponding coupled differential equations. Considering a surface coverage of  $C$  active sites in sites  $\text{cm}^{-2}$ , the corresponding current is the following, where  $q$  is the charge of an electron:

$$I(t) = Cq \frac{\partial[e(t)]}{\partial t} \quad (\text{Eq. S34})$$

### Electroadsorption analysis

An electroadsorption analysis model was developed by assuming that each elementary step was under thermodynamic equilibrium. Each elementary 1-electron reaction step can then be described by the Nernst equation:

$$E = E_i^0 - \frac{RT}{F} \ln [Q_i] \quad (\text{Eq. S35})$$

where  $E$  is potential,  $E_i^0$  is the standard potential,  $R$  is the ideal gas constant,  $T$  is temperature,  $F$  is Faraday's constant, and  $Q_i$  is the reaction quotient for each elementary step. The activity of all aqueous species was set to 1 to match the conditions in an idealized 1.0 M acid. For a 1-electron Nernstian surface-bound electrochemical reaction, such as the formation of \*OH from  $H_2O$ , the surface coverage can be analytically solved as the following:

$$\Gamma_{S-OH}(E) = \Gamma_{S-OH,s} \frac{e^{\frac{F}{RT}(E-E_1^0)}}{1 + e^{\frac{F}{RT}(E-E_1^0)}} \quad (\text{Eq. S36})$$

Where  $\Gamma_{S-OH}$  is the surface coverage of the S-OH intermediate,  $\Gamma_{S-OH,s}$  is the saturated surface coverage of S-OH, and  $F$ ,  $R$ ,  $T$ ,  $E$ , and  $E_1^0$  have their usual meaning. The capacitive current associated with this surface reaction can be obtained via the following equation:

$$I_{cap}(E) = \frac{\partial Q(E)}{\partial t} = \frac{\partial Q(E)}{\partial E} \frac{\partial E(t)}{\partial t} = vq \frac{\partial \Gamma_{S-OH}(E)}{\partial E} \quad (\text{Eq. S37})$$

Where  $Q$  is the charge passed as a function of potential,  $q$  is the charge of an electron, and  $E(t)$  is the applied voltage over time. For a linear sweep during a cyclic voltammogram,  $\frac{\partial E(t)}{\partial t}$  corresponds to the scan rate ( $v$ ) of the experiment. For a Nernstian reaction, the resulting peak shape is the following:

$$I_{cap,ernst}(E) = vq\Gamma_{S-OH,s} \frac{\frac{F}{RT} e^{\frac{F}{RT}(E-E_1^0)}}{\left[1 + e^{\frac{F}{RT}(E-E_1^0)}\right]^2} \quad (\text{Eq. S38})$$

Experimental peak shapes exhibit broadening that cannot be accurately captured by a single idealized Nernstian reaction. Adsorbate-adsorbate interactions have been proposed to account for this observation, and sample heterogeneity at the nanoscale could also account for broadening.<sup>2, 9</sup> We propose that heterogeneity could be accounted for via the following equation:

$$I_{cap}(E) = vq\Gamma_{S-OH,s} \int_{-\infty}^{\infty} P(\epsilon) \frac{\frac{F}{RT} e^{\frac{F}{RT}(E-\epsilon)}}{\left[1 + e^{\frac{F}{RT}(E-\epsilon)}\right]^2} d\epsilon \quad (\text{Eq. S39})$$

Where  $P(\epsilon)$  is a normalized distribution function that describes the distribution of standard electrochemical potentials for electron transfer on an electrocatalyst surface. In this framework, each electron-transfer reaction is treated as a collection of idealized Nernstian reactions that are weighted by a probability distribution. Numerical solutions can be obtained for this model for any required distribution function, but to simplify further analysis, the following simplification will be made:

$$\int_{-\infty}^{\infty} P(\varepsilon) \frac{\frac{F}{RT} e^{\frac{F}{RT}(E-\varepsilon)}}{\left[1 + e^{\frac{F}{RT}(E-\varepsilon)}\right]^2} d\varepsilon \approx \frac{F}{\beta RT} \frac{e^{\frac{F}{\beta RT}(E-\varepsilon)}}{\left[1 + e^{\frac{F}{\beta RT}(E-\varepsilon)}\right]^2} \quad (\text{Eq. S40})$$

Where  $\beta$  is the heterogeneity parameter. A  $\beta$  value of 1 corresponds to a Nernstian process with no deviation in the standard potential for the reaction on a surface. A  $\beta$  greater than 1 will result in peak broadening but will not change the overall charge passed during the electron transfer step. Supplementary Fig. 16 shows a comparison between the analytical result obtained with the heterogeneity parameter and a reaction modeled by a normal distribution function. At 298.15 K, the following empirical relationship was obtained between the standard deviation of a population ( $\sigma$ ) between 0 and 0.25 V and  $\beta$ :

$$\sigma \approx 0.0249(\beta - 1)^{1.1186} + 0.0455(\beta - 1)^{0.4634} \text{ (V)} \quad (\text{Eq. S41})$$

The following parameter is defined to simplify subsequent equations:

$$z_i = e^{\frac{F}{\beta RT}(E - E_i^0)} \quad (\text{Eq. S42})$$

Where  $F$  is Faraday's constant,  $E$  is the applied potential,  $R$  is the ideal gas constant,  $T$  is temperature,  $E_i^0$  is the standard potential, and  $\beta$  is the heterogeneity parameter.

For  $N$  number of coupled 1-electron reactions, the normalized surface coverage of the  $S$  empty active site is the following:

$$\theta_S = \frac{\Gamma_S}{\Gamma_{S,sat}} = \frac{1}{1 + \sum_{j=1}^N \prod_{i=1}^j z_j} \quad (\text{Eq. S43})$$

Where  $\Gamma_S$  is the surface coverage and  $\Gamma_{S,sat}$  is the saturated surface coverage, and  $\Sigma$  and  $\Pi$  correspond to sums and product sums, respectively. The normalized surface coverage for the intermediate  $i$  is given by:

$$\theta_i = \frac{\Gamma_i}{\Gamma_{i,sat}} = \frac{\Gamma_S}{\Gamma_{S,sat}} \prod_{j=1}^i z_j \quad (\text{Eq. S44})$$

The resulting functions that describe surface coverage as a function of voltage are analytical, enabling exhaustive computation of parameters that fit experiment data. For the OER, three reaction intermediates (\*OH, \*O, and \*OOH) were considered, resulting in the following equations:

$$\theta_S = \frac{\Gamma_S}{\Gamma_{S,sat}} = \frac{1}{1 + z_1 + z_1 z_2 + z_1 z_2 z_3} \quad (\text{Eq. S45})$$

$$\theta_{S-OH} = \frac{\Gamma_{S-OH}}{\Gamma_{S-OH,sat}} = \frac{z_1}{1 + z_1 + z_1z_2 + z_1z_2z_3} \quad (\text{Eq. S46})$$

$$\theta_{S-O} = \frac{\Gamma_{S-O}}{\Gamma_{S-O,sat}} = \frac{z_1z_2}{1 + z_1 + z_1z_2 + z_1z_2z_3} \quad (\text{Eq. S47})$$

$$\theta_{S-OOH} = \frac{\Gamma_{S-OOH}}{\Gamma_{S-OOH,sat}} = \frac{z_1z_2z_3}{1 + z_1 + z_1z_2 + z_1z_2z_3} \quad (\text{Eq. S48})$$

Each step can be allowed to have an independent areal surface coverage,  $\Gamma_{s,i}$ , and the overall charge passed due to electroadsorption is the following:

$$Q_{ads}(E) = q\theta_{S-OH}\Gamma_{S-OH} + q\theta_{S-O}[\Gamma_{S-OH} + \Gamma_{S-O}] + q\theta_{S-OOH}[\Gamma_{S-OH} + \Gamma_{S-O} + \Gamma_{S-OOH}] \quad (\text{Eq. S49})$$

The experimentally observed capacitance associated with electroadsorption can be determined via the following equation:

$$C_{ads}(E) = \frac{\partial Q_{ads}(E)}{\partial E} \quad (\text{Eq. S50})$$

Where  $\frac{\partial Q_{ads}(V)}{\partial V}$  is the derivative of the analytical  $Q_{ads}(E)$  function versus voltage. The overall capacitive current observed will include contributions from double layer capacitance which was modeled as a perfect capacitor:

$$C(E) = C_{DL} + C_{ads}(E) \quad (\text{Eq. S51})$$

where  $C_{DL}$  is the double-layer capacitance. For the nanocrystals studied herein, the electroadsorption current was modeled as exhibiting contributions from two distinct active sites from (110) and (111)/(112) crystallographic facets:

$$C(E) = C_{DL} + C_{(110)}(E) + C_{(111)/(112)}(E) \quad (\text{Eq. S52})$$

The overall current at a given electrode scan rate is obtained via the following equation:

$$I(E) = C(E) \frac{\partial E(t)}{\partial t} = vC(E) \quad (\text{Eq. S53})$$

The site density for each catalyst was determined from the ECSA-normalized  $\Gamma_{S-OH,sat}$  for the catalytic active site with the most optimal energetics for the OER, which corresponded to the (110) active sites in all cases. Turn-over frequencies (TOF) were determined by dividing the experimentally observed current density by the 4 times the site density, accounting for the four electron transfer steps associated with the OER. Site density corresponds to the number of electrochemically active (110) sites determined from electroadsorption measurements normalized to the electrochemically active surface area, representing the exposed surface area of the nanocrystals. It was assumed that the site concentration equaled the \*OH concentration and that all catalysts exhibited a specific capacitance of 0.04 mF cm<sup>-2</sup>.

## Kinetic model

The kinetic analysis was performed with the fourth electron transfer step being rate-determining. The forward rate constant is expressed in Eq. S56.

$$k_f = k_0 e^{-\alpha \frac{(E - E_{rds})}{V_t}} \quad (\text{Eq. S56})$$

where  $E_{rds}$  represents the potential of the rate-determining step. The catalytic current was simulated to fit the data with the following formula that considers the potential-dependent \*OOH coverage determined from electroadsorption analysis.

$$I_{cat}(E) = 4qk_f[S - OOH] = \frac{z_1 z_2 z_3 4qk_0 \Gamma_{S - OOH, sat}}{1 + z_1 + z_1 z_2 + z_1 z_2 z_3} e^{-\alpha \frac{(E - E_{rds})}{V_t}} \quad (\text{Eq. S57})$$

The models described herein were implemented in MATLAB to find numerical solutions that could adequately describe the observed data. The MultiStart function was used to exhaustively search parameters that would fit to experimental data. For (111)/(112) active sites, the intermediate binding energy was allowed vary from the minimum measured experimental potential (~0.2 to 0.3 V vs. RHE) to 1.1 V vs. RHE, and the intermediate binding energies for (110) were allowed to vary from 0.8 V vs. RHE to the maximum measured experimental potential (~ 1.4 to 1.6 V vs. RHE). The  $\beta$  parameter was allowed to vary between 1 and 3, corresponding to intermediate standard deviations of approximately 0.0 to 0.117 eV. Relative site density of \*O and \*OOH intermediates was allowed to vary from 0.25 to 1.25 versus the \*OH site density. The steady-state kinetics were modeled by contributions from (110) active sites. The charge transfer coefficient  $\alpha$  was allowed to vary from 0.1 to 2, and  $E_{rds}$  was allowed to vary from 0 to 3 V.

## **Density Functional Theory**

Density functional theory (DFT) calculations were performed using the Vienna Ab initio Simulation Package (VASP). The projector augmented wave (PAW) potentials (Ru\_pv, Mn\_pv, Fe, O, H) were employed and exchange-correlation functionals were described using the PBE scheme. A plane-wave cutoff energy of 400 eV and a 3 x 2 x 1 Monkhorst-Pack k-point grid was used in all calculations. Smearing was introduced using the first-order Methfessel-Paxton method with a smearing width of 0.2 eV. The truncation criterion for electronic steps was chosen to be  $10^{-6}$  eV. All calculations were performed with spin polarization and precision mode was set to accurate. The starting magnetization for Mn and Fe atoms were set to 5.0 and 4.0 respectively, and 0 for all other atoms.

The rutile RuO<sub>2</sub>(110) surfaces were modeled as periodic four-layer slabs with a 2 x 3 surface supercell (9.37 x 12.73 Å<sup>2</sup>) and a vacuum gap of about 18 Å. The bottom two layers were kept fixed, and all other atoms were relaxed until the forces were less than 0.05 eV/Å. The structures for single- and dual-site doping are shown in Supplementary Fig. 24.

## **Proton exchange membrane water electrolysis devices construction**

Proton exchange membrane water electrolysis (PEMWE) was used to measure the stability of the synthesized electrocatalysts under operation. To make the catalyst ink, 5.4  $\mu\text{L}$  of Nafion and 4.6  $\mu\text{L}$  of DI water were added for every mg of powder catalyst. The catalyst ink was sonicated for 45 minutes. The catalyst ink was drop-cast on a 1 x 1 cm PTFE sheet in 10  $\mu\text{L}$  aliquots and dried using a heat gun between each application. A 5 x 5 cm Nafion N115 (Ion Power) membrane was cut. The catalyst was transferred from the PTFE sheet to the Nafion membrane by hot pressing at 150  $^{\circ}\text{C}$  for 180 s. The area of the catalyst was determined through the ImageJ software using an optical scanner. The catalyst loadings were determined to be 3.8 mg per  $\text{cm}^{-2}$  for FeMn-RuO<sub>x</sub> and 2.7 mg  $\text{cm}^{-2}$  for RuO<sub>2</sub> synthesized at 500  $^{\circ}\text{C}$ . The catalyst coated membrane was hydrated in DI water at 80  $^{\circ}\text{C}$  for 1 hour with catalyst side facing up. To construct the electrolyzer, a 1.2 x 1.2 cm platinized titanium sheet (thermally platinized low porosity titanium fiber felt, FuelCell store) was cut and used as the anode in contact with the catalyst side of the Nafion membrane and a 1.2 x 1.2 cm platinized carbon paper (paper GDE, 0.5mg  $\text{cm}^{-2}$  PtC 60%) was cut and used as the cathode. With a pumping speed of 50  $\text{rev min}^{-1}$ , DI water at 45  $^{\circ}\text{C}$  was flowed through the electrolyzer to flush air out of the system. An activation was performed with chronopotentiometry at 100  $\text{mA cm}^{-2}$  to remove the residual oxygen in the set up. The stability tests were performed at 100  $\text{mA cm}^{-2}$  for both FeMn-RuO<sub>x</sub> and RuO<sub>2</sub>. Titanium flow fields that were fabricated in-house were also utilized for FeMn-RuO<sub>x</sub> synthesized under 500  $^{\circ}\text{C}$  and commercial RuO<sub>2</sub>. The catalyst inks were prepared by adding 2.7  $\mu\text{L}$  of Nafion and 9.2  $\mu\text{L}$  of water for every mg of catalyst, which were dispersed via sonication. On a Nafion N212 membrane (Ion Power), catalyst inks were drop-cast and dried with vacuum pulling on a vacuum plate. The loading amount was 2 mg of catalyst. The area of the catalyst was measured using the same protocol mentioned above. To construct the electrolyzer, a 1.2 x 1.2 cm platinized titanium sheet was cut and used as the anode in contact with the catalyst side of the Nafion membrane and a 1.2 x 1.2 cm platinized carbon paper was cut and used as the cathode. With a pumping speed of 90  $\text{rev min}^{-1}$ , DI water at 80  $^{\circ}\text{C}$  was flowed through the electrolyzer to flush air out of the system. An activation was performed with chronopotentiometry at 100  $\text{mA cm}^{-2}$  to remove the residual oxygen in the set up. Next, a cyclic voltammetry protocol with a potential range of 0 V to 2 V at 10  $\text{mV s}^{-1}$  was taken for both FeMn-RuO<sub>x</sub> and commercial RuO<sub>2</sub>.

### **Pre and post OER characterization**

#### *FeMn-RuO<sub>x</sub>*

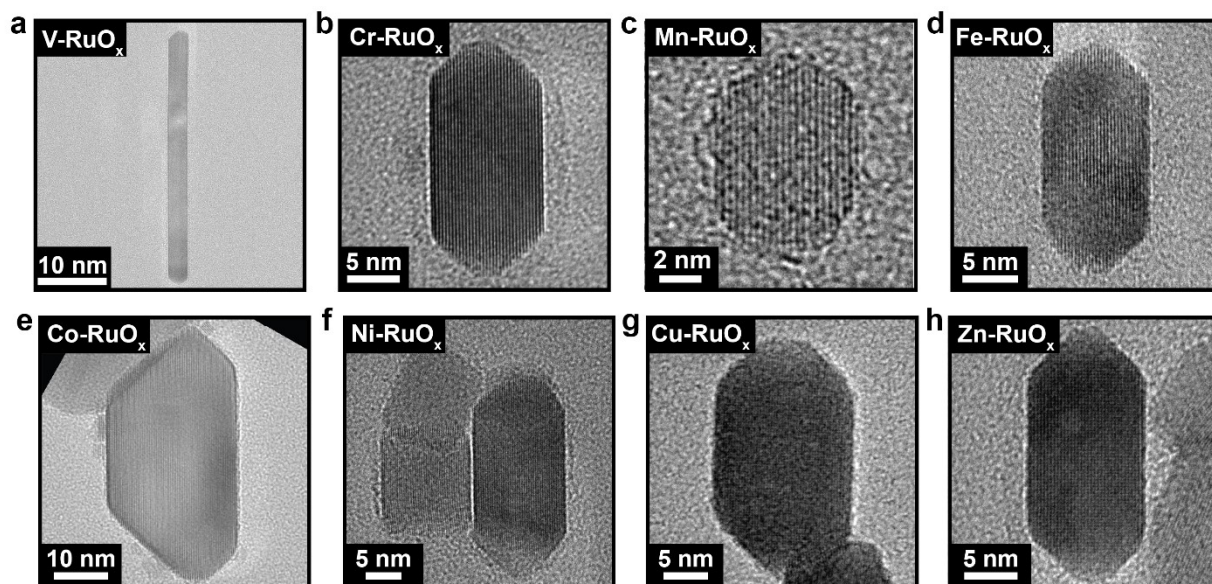
Pre and post mortem FeMn-RuO<sub>x</sub> samples were made using the following steps. Catalyst ink was made by adding 10  $\mu\text{L}$  of IPA for every mg of nano-powder, which was fully dispersed through 15 minutes sonication. In 2  $\mu\text{L}$  aliquots, the catalyst ink was drop-cast onto a titanium foil and dried under vacuum. This process was repeated four times. Electrochemical tests were performed in a three-electrode set up with bubbled ultra-high purity oxygen, where the working electrode is the catalyst-coated titanium foil, the counter electrode is a carbon rod, and the reference electrode is an Ag/AgCl electrode calibrated to 0.188 V versus the reversible hydrogen electrode (RHE). The electrolyte was freshly prepared 1.0 M perchloric acid. For both post FeMn-RuO<sub>x</sub> samples, electrochemical impedance spectroscopy (EIS) was conducted to determine the series resistance with frequency ranging from 1 MHz to 1 Hz. For the post FeMn-RuO<sub>x</sub> sample, cyclic voltammetry (CV) with potential ranges from 0 to 1.45 V versus Ag/AgCl was performed at scan rate ( $v$ ) of 1000  $\text{mV s}^{-1}$  and repeated 2 times. The post sample was rinse with DI water and dried under the vacuum prior to XPS data acquisition.

SEM-EDS data was collected for the pre and post samples following the protocol mentioned above. XPS data was collected for the pre and post samples following the XPS protocol mentioned above with the following modifications. Region scans for Mn 2p and Fe 2p were collected averaging 20 scans.

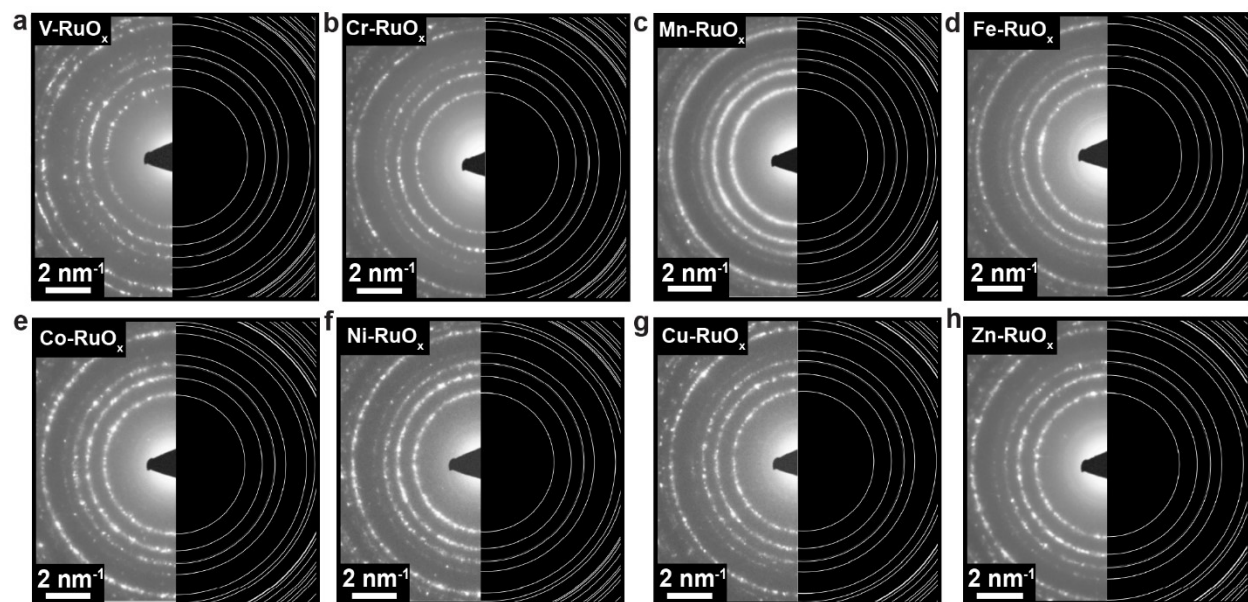
#### *M-RuO<sub>x</sub>*

Catalyst inks for RuO<sub>2</sub>, V-RuO<sub>x</sub> and Mn-RuO<sub>x</sub> nanocrystalline samples synthesized at 700 °C were prepared by adding 83.5 μL of H<sub>2</sub>O, 35.5 μL of IPA and 6 μL of Nafion for every mg of nano-powder. The catalyst inks were sonicated for 45 minutes to enable full dispersion. Electrochemical tests were performed using a rotating disk electrode operated at 2000 rpm and a three-electrode system at room temperature (25 °C) using a Bio-logic potentiostat. The counter electrode was a platinum electrode (Pine Research), the reference electrode was an Ag/AgCl electrode calibrated to 0.188 V versus RHE, the working electrode was a glassy carbon rotating disk electrode (RDE), and the electrolyte was 1.0 M perchloric acid. Ultrahigh purity oxygen was bubbled during the experiments to saturate the electrolyte. The catalyst ink was drop-cast onto the RDE tip with 250 μg cm<sup>-2</sup> loadings. Electrochemical impedance spectroscopy (EIS) was conducted to determine the series resistance with frequency ranging from 1 MHz to 1 Hz. Next, cyclic voltammetry (CV) with potential ranges from 0 to 1.45 V versus Ag/AgCl was performed at scan rate (v) of 1000 mV s<sup>-1</sup> and repeated 99 times. Catalyst powders for all samples were recollected from the RDE tip using a plastic spatula and dispersed in DI water. After 10 minutes of sonication, 5 μL of each sample was drop-cast onto a gold TEM grid (Electron Microscopy Sciences, CF200-AU, carbon coated, 200 mesh) and dried under vacuum. TEM images were collected using a 200kV FEG (field emission gun) Thermo Fisher Talos F200X microscope located at the Analytical Instrumentation Facility located at North Carolina State University.

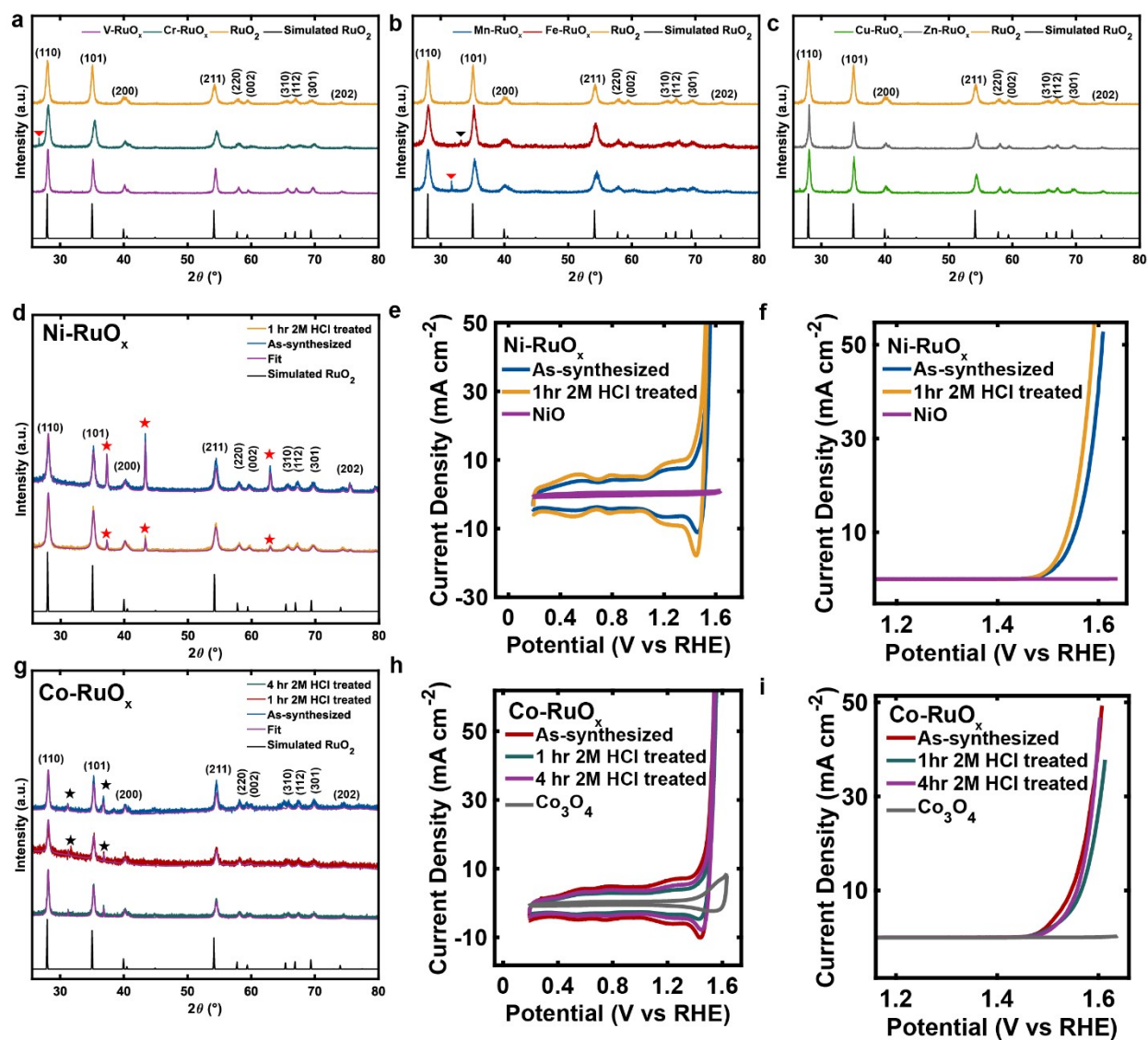
**Supplementary Figures**



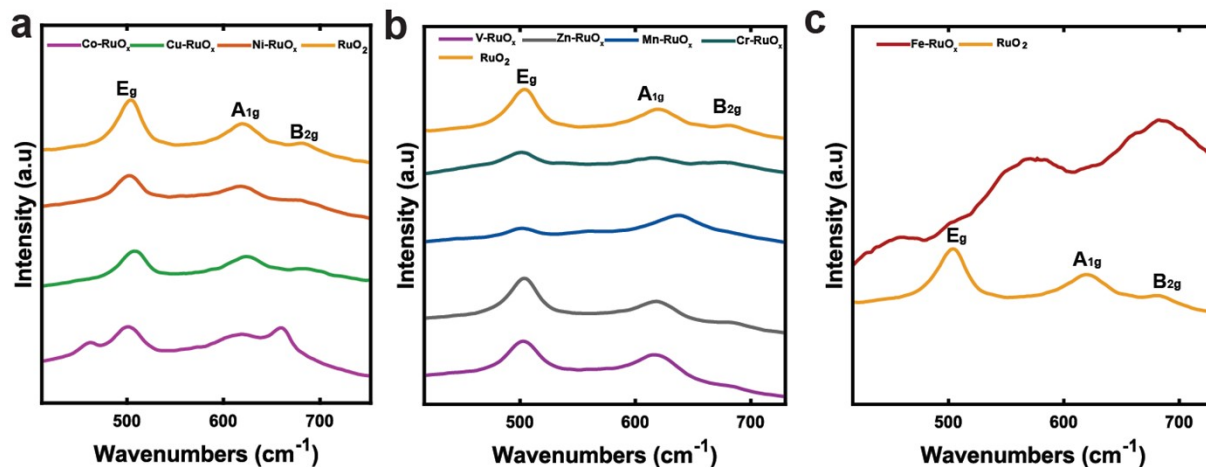
**Supplementary Fig. 1.** HR-TEM images of (a) V-RuO<sub>x</sub>, (b) Cr-RuO<sub>x</sub>, (c) Mn-RuO<sub>x</sub>, (d) Fe-RuO<sub>x</sub>, (e) Co-RuO<sub>x</sub>, (f) Ni-RuO<sub>x</sub>, (g) Cu-RuO<sub>x</sub> and (h) Zn-RuO<sub>x</sub> nanocrystals synthesized at 700 °C.



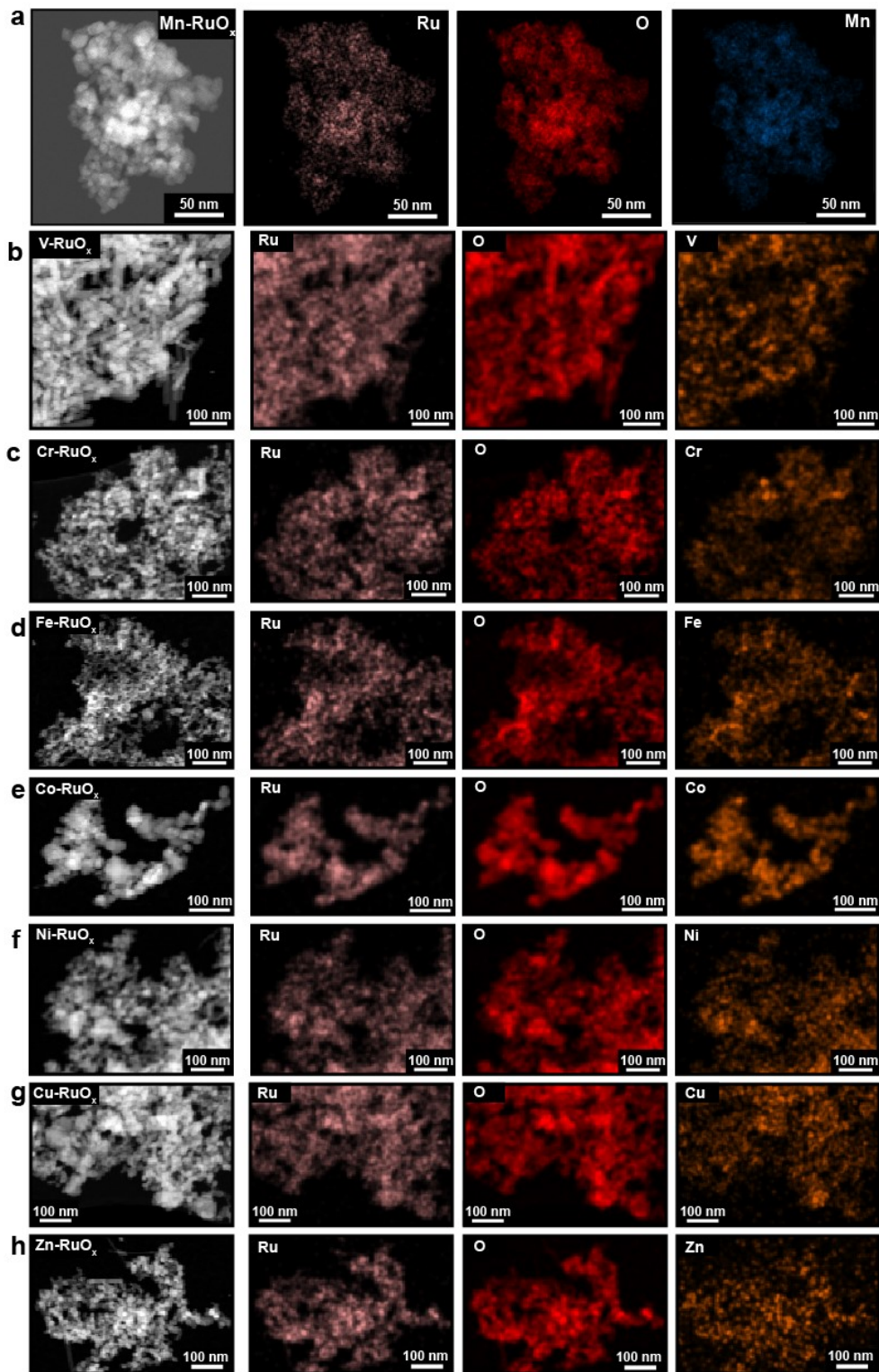
**Supplementary Fig. 2.** SAED of  $\text{RuO}_2$  and  $\text{M-RuO}_x$  nanocrystals synthesized at  $700\text{ }^\circ\text{C}$ . Experimental SAED (left) and database  $\text{RuO}_2$  (ICSD-56007) ED (right) of (a)  $\text{V-RuO}_x$ , (b)  $\text{Cr-RuO}_x$ , (c)  $\text{Mn-RuO}_x$ , (d)  $\text{Fe-RuO}_x$ , (e)  $\text{Co-RuO}_x$ , (f)  $\text{Ni-RuO}_x$ , (g)  $\text{Cu-RuO}_x$  and (h)  $\text{Zn-RuO}_x$ .



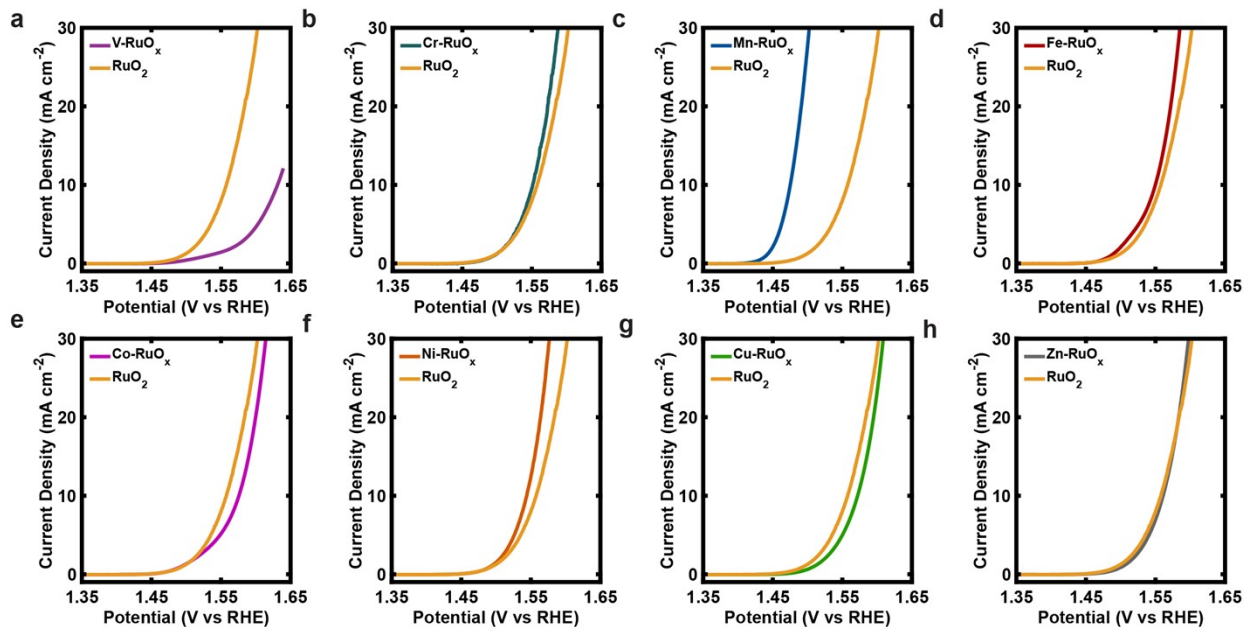
**Supplementary Fig. 3.** XRD and electrochemical characterization of RuO<sub>2</sub> and M-RuO<sub>x</sub> nanocrystalline samples synthesized at 700 °C. Experimental XRD patterns of RuO<sub>2</sub> and simulated XRD patterns of database RuO<sub>2</sub> (ICSD-56007) plotted with experimental XRD patterns of (a) V-RuO<sub>x</sub>, Cr-RuO<sub>x</sub>, (b) Mn-RuO<sub>x</sub>, Fe-RuO<sub>x</sub>, (c) Cu-RuO<sub>x</sub> and Zn-RuO<sub>x</sub>. (d) Experimental XRD patterns of 1 hour 2M HCl treated and as-synthesized Ni-RuO<sub>x</sub> plotted with simulated RuO<sub>2</sub> XRD pattern (ICSD-56007). (e) IR-corrected CVs collected at 1V s<sup>-1</sup>, and (f) IR-corrected average current density-voltage profiles collected at 10 mV s<sup>-1</sup> of 1 hour 2M HCl treated, as-synthesized Ni-RuO<sub>x</sub> and commercial NiO. (g) Experimental XRD patterns of 1 hour 2M HCl treated, 4 hours HCl treated, and as-synthesized Co-RuO<sub>x</sub> plotted with simulated RuO<sub>2</sub> XRD pattern (ICSD-56007). (h) IR-corrected CVs collected at 1V s<sup>-1</sup>, and (i) IR-corrected average current density-voltage profiles collected at 10 mV s<sup>-1</sup> of 1 hour 2M HCl treated, 4 hours HCl treated, as-synthesized Co-RuO<sub>x</sub> and commercial Co<sub>3</sub>O<sub>4</sub>. Red triangles are attributed to residual NaCl; black triangle is attributed to residual Na<sub>2</sub>SO<sub>4</sub>; red stars are attributed to NiO; black stars are attributed to Co<sub>3</sub>O<sub>4</sub>.



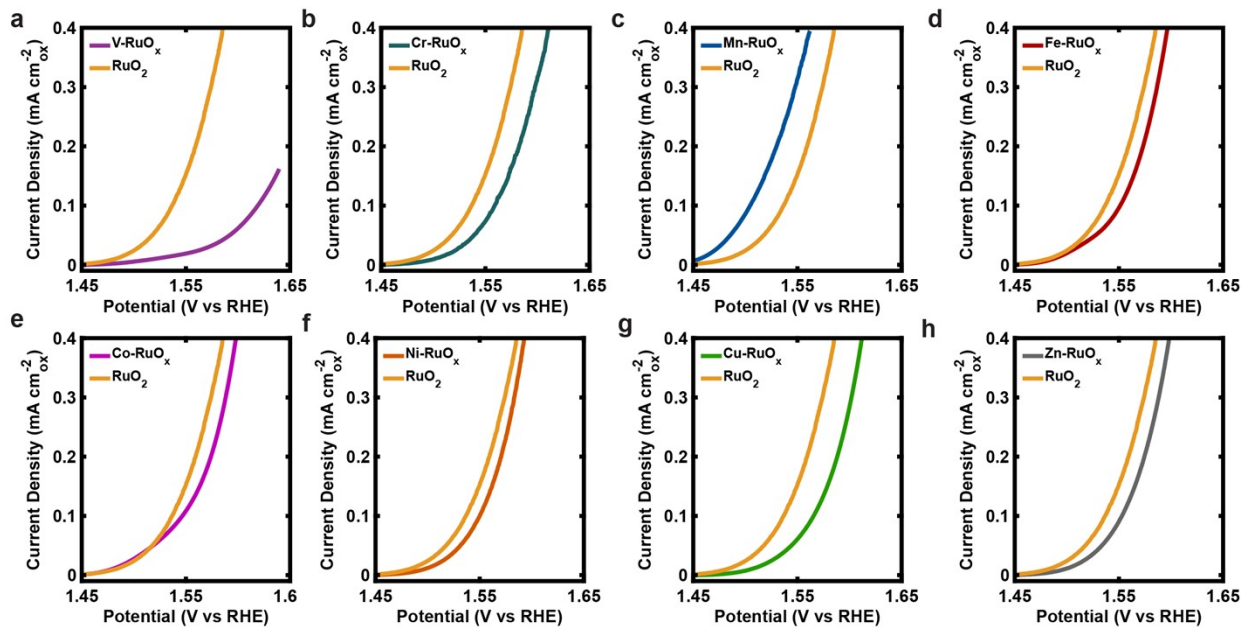
**Supplementary Fig. 4.** Raman spectra of RuO<sub>2</sub> and M-RuO<sub>x</sub> nanocrystalline samples synthesized at 700 °C with vibration modes labeled. Raman spectra of RuO<sub>2</sub> plotted with that of (a) Co-RuO<sub>x</sub>, Cu-RuO<sub>x</sub>, Ni-RuO<sub>x</sub>, (b) V-RuO<sub>x</sub>, Zn-RuO<sub>x</sub>, Mn-RuO<sub>x</sub>, Cr-RuO<sub>x</sub>, (c) Fe-RuO<sub>x</sub>.



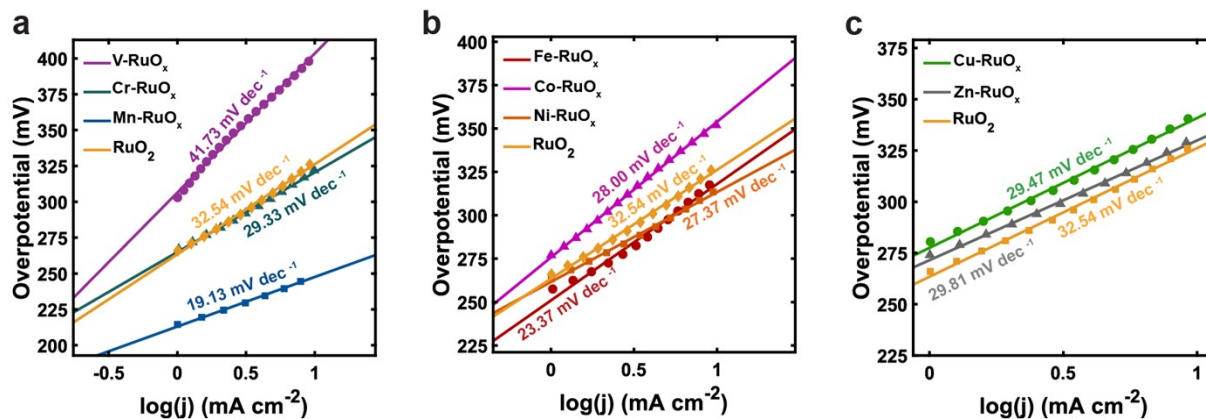
**Supplementary Fig. 5.** STEM-EDS elemental distributions of M-RuO<sub>x</sub> nanocrystals synthesized at 700 °C. HAADF images and elemental distributions of (a) Mn-RuO<sub>x</sub>, (b) V-RuO<sub>x</sub>, (c) Cr-RuO<sub>x</sub>, (d) Fe-RuO<sub>x</sub>, (e) Co-RuO<sub>x</sub>, (f) Ni-RuO<sub>x</sub>, (g) Cu-RuO<sub>x</sub> and (h) Zn-RuO<sub>x</sub>.



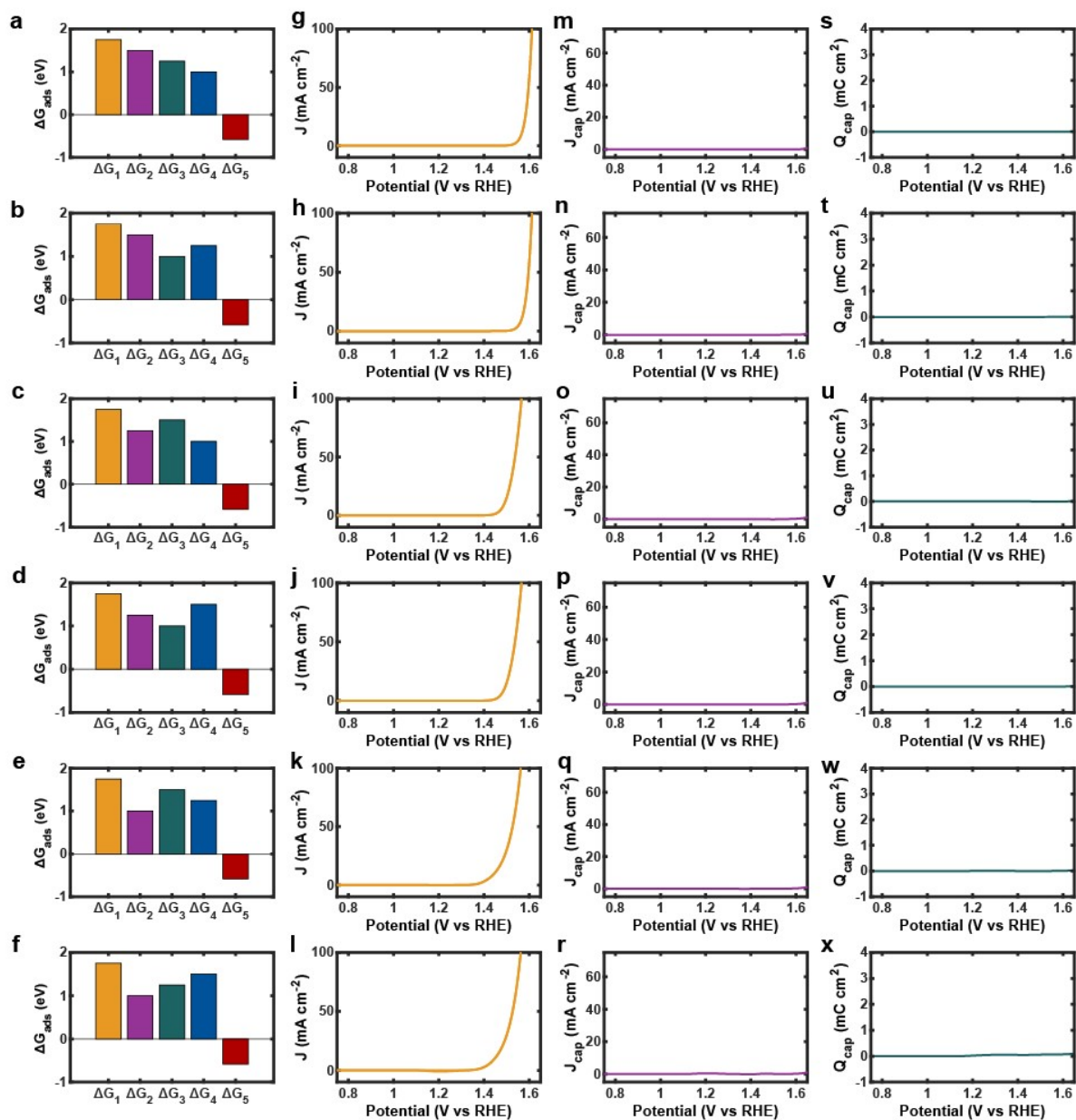
**Supplementary Fig. 6.** IR-corrected steady-state current from averaged CVs collected at  $10 \text{ mV s}^{-1}$  scan rate of  $\text{RuO}_2$  and  $\text{M-RuO}_x$  electrocatalysts synthesized at  $700^\circ\text{C}$ . Plots of average IR-corrected current density versus potential of  $\text{RuO}_2$  plotted with that of (a)  $\text{V-RuO}_x$ , (b)  $\text{Cr-RuO}_x$ , (c)  $\text{Mn-RuO}_x$ , (d)  $\text{Fe-RuO}_x$ , (e)  $\text{Co-RuO}_x$ , (f)  $\text{Ni-RuO}_x$ , (g)  $\text{Cu-RuO}_x$ , (h)  $\text{Zn-RuO}_x$ .



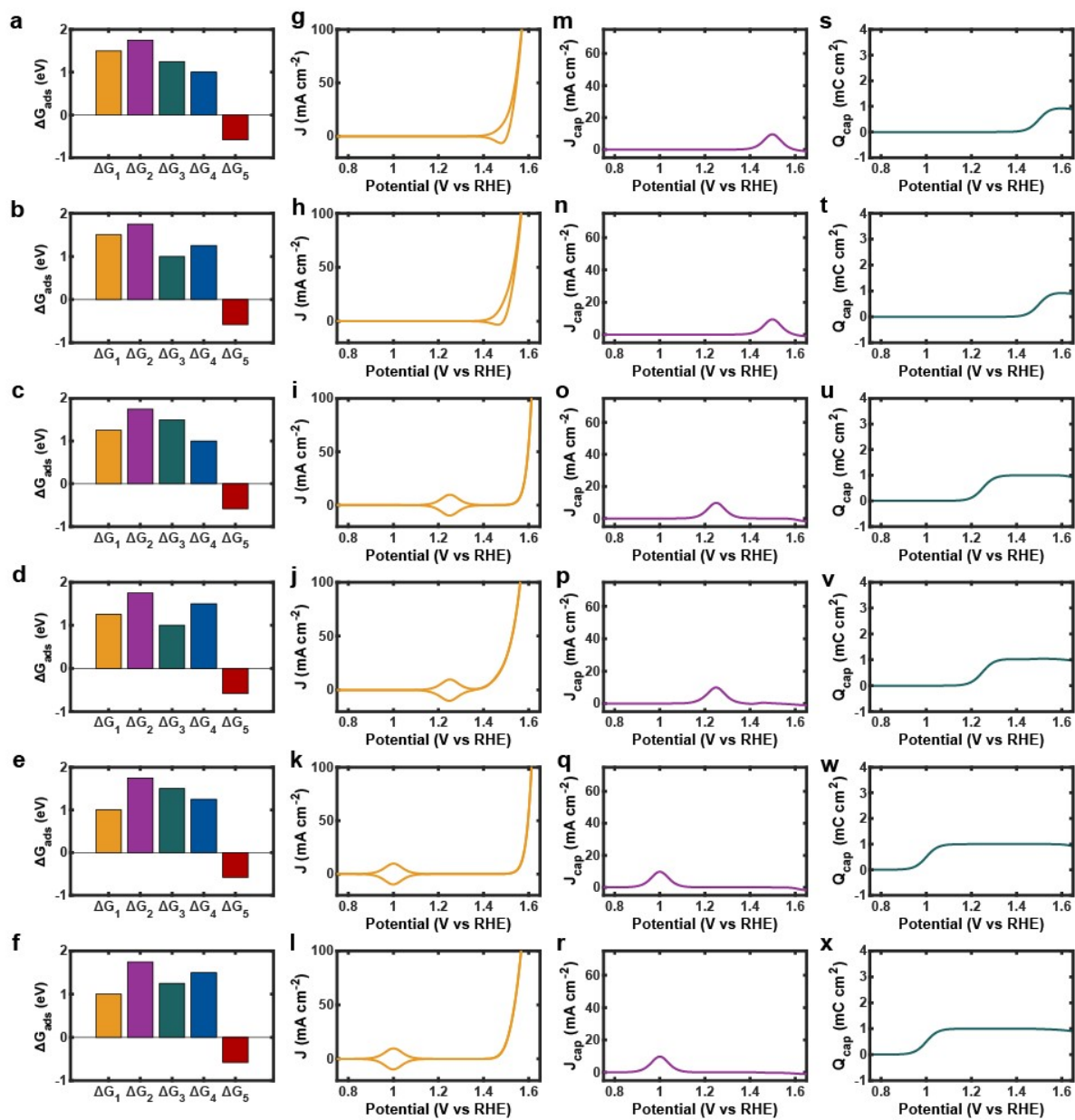
**Supplementary Fig. 7.** ECSA-corrected steady-state current from averaged CVs collected at  $10 \text{ mV s}^{-1}$  scan rate of  $\text{RuO}_2$  and  $\text{M-RuO}_x$  electrocatalysts synthesized at  $700^\circ\text{C}$ . Plots of average ECSA-corrected current density versus potential of  $\text{RuO}_2$  plotted with that of (a)  $\text{V-RuO}_x$ , (b)  $\text{Cr-RuO}_x$ , (c)  $\text{Mn-RuO}_x$ , (d)  $\text{Fe-RuO}_x$ , (e)  $\text{Co-RuO}_x$ , (f)  $\text{Ni-RuO}_x$ , (g)  $\text{Cu-RuO}_x$ , (h)  $\text{Zn-RuO}_x$ .



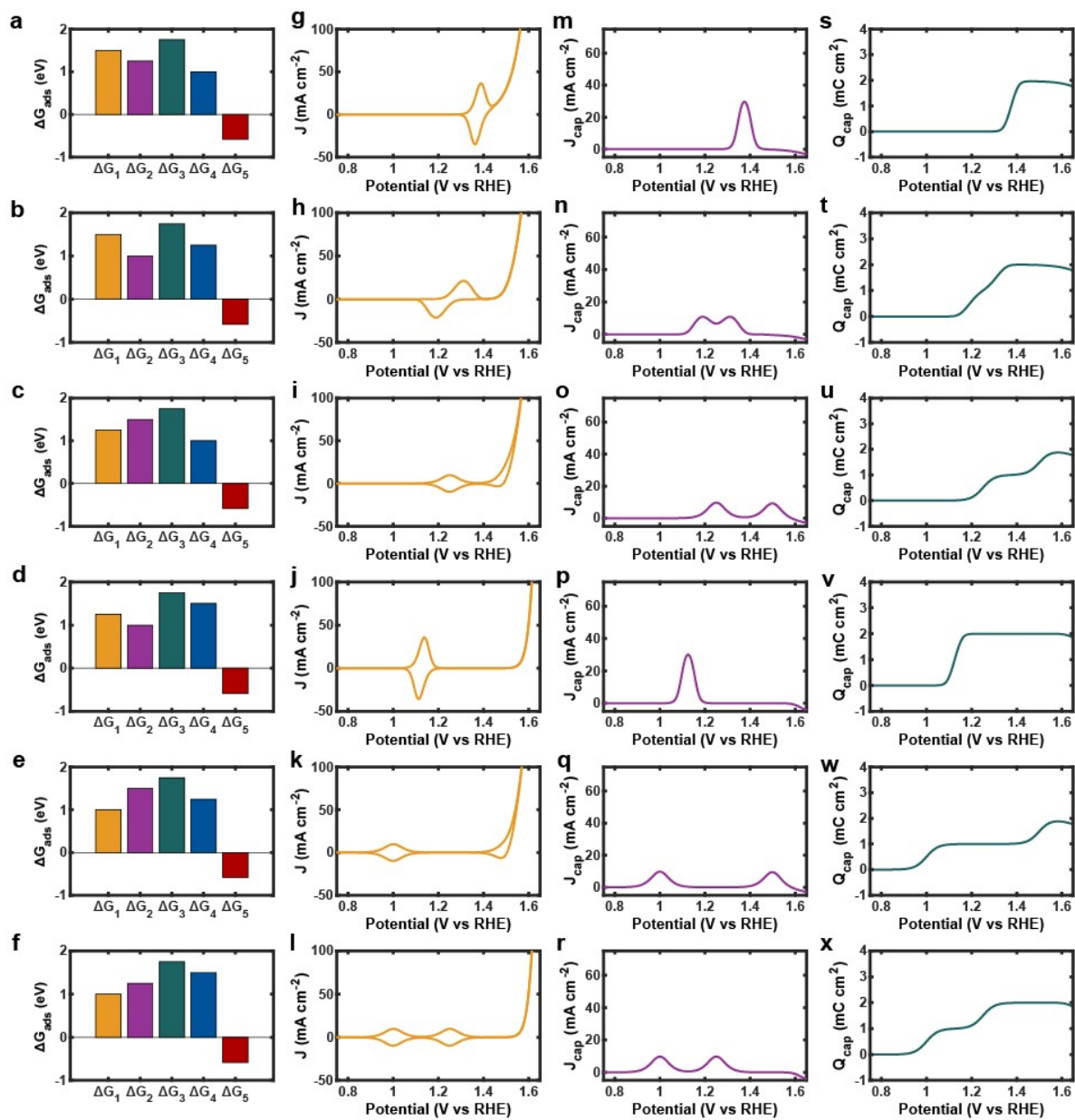
**Supplementary Fig. 8.** Tafel plots of RuO<sub>2</sub> and M-RuO<sub>x</sub> electrocatalysts synthesized at 700 °C with Tafel slopes labeled. Tafel plot of RuO<sub>2</sub> plotted with that of a) V-RuO<sub>x</sub>, Cr-RuO<sub>x</sub>, Mn-RuO<sub>x</sub>, b) Fe-RuO<sub>x</sub>, Co-RuO<sub>x</sub>, Ni-RuO<sub>x</sub>, c) Cu-RuO<sub>x</sub>, and Zn-RuO<sub>x</sub>.



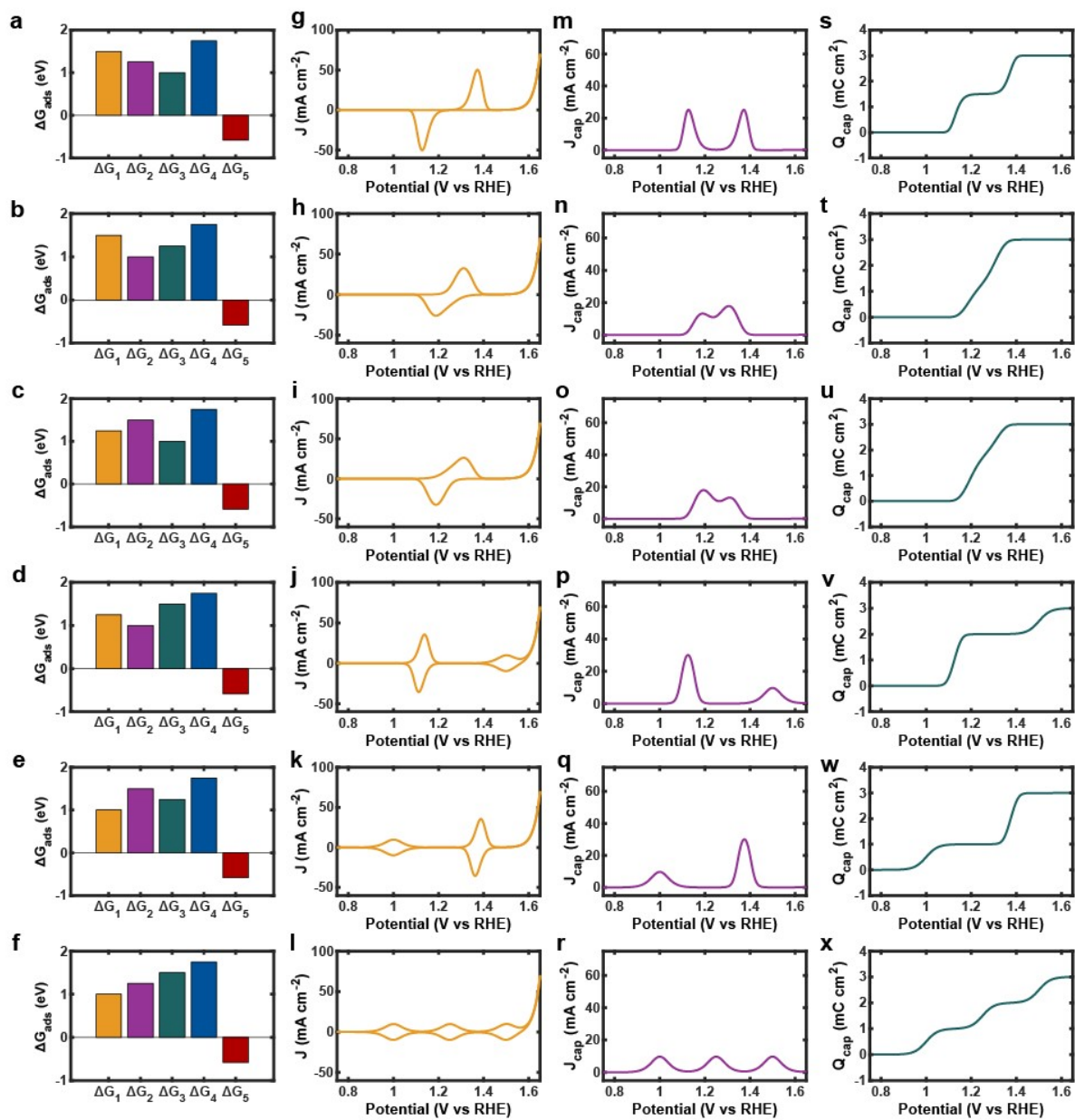
**Supplementary Fig. 9.** Summary of simulated microkinetic model with equation S8 being the rate-determining step. (a-f) Summary of the simulated  $\Delta G$  with different permutations. (g-l) Simulated CVs for different permutations of  $\Delta G$  from a to f. (m-r) Simulated electroadsorption current-voltage profiles of different permutations of  $\Delta G$  from a to f. (s-x) Simulated charge-potential profiles of different permutations of  $\Delta G$  from a to f.



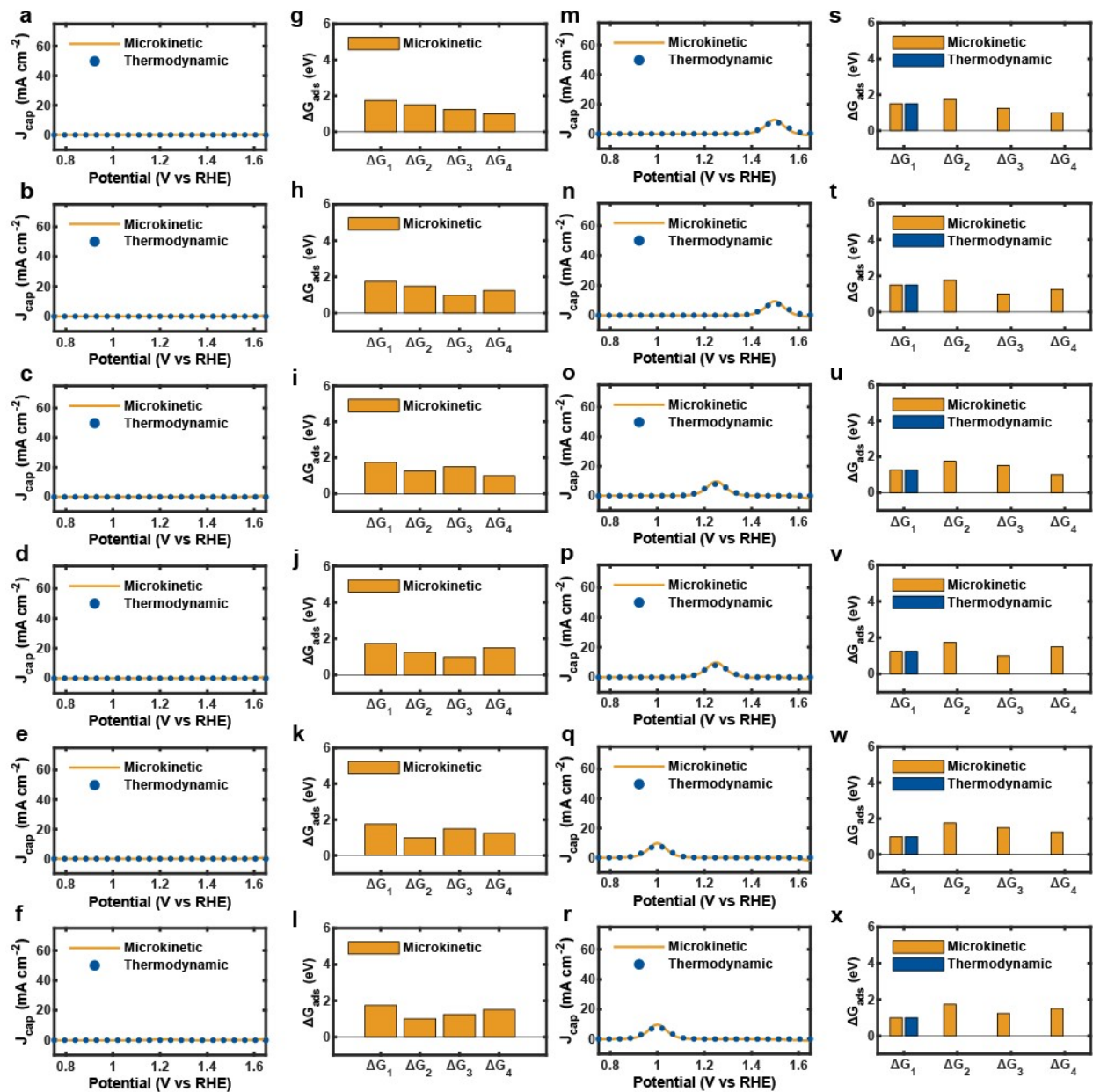
**Supplementary Fig. 10.** Summary of simulated microkinetic model with equation S9 being the rate-determining step. (a-f) Summary of the simulated  $\Delta G$  with different permutations. (g-l) Simulated CVs for different permutations of  $\Delta G$  from a to f. (m-r) Simulated electroadsorption current-voltage profiles of different permutations of  $\Delta G$  from a to f. (s-x) Simulated charge-potential profiles of different permutations of  $\Delta G$  from a to f.



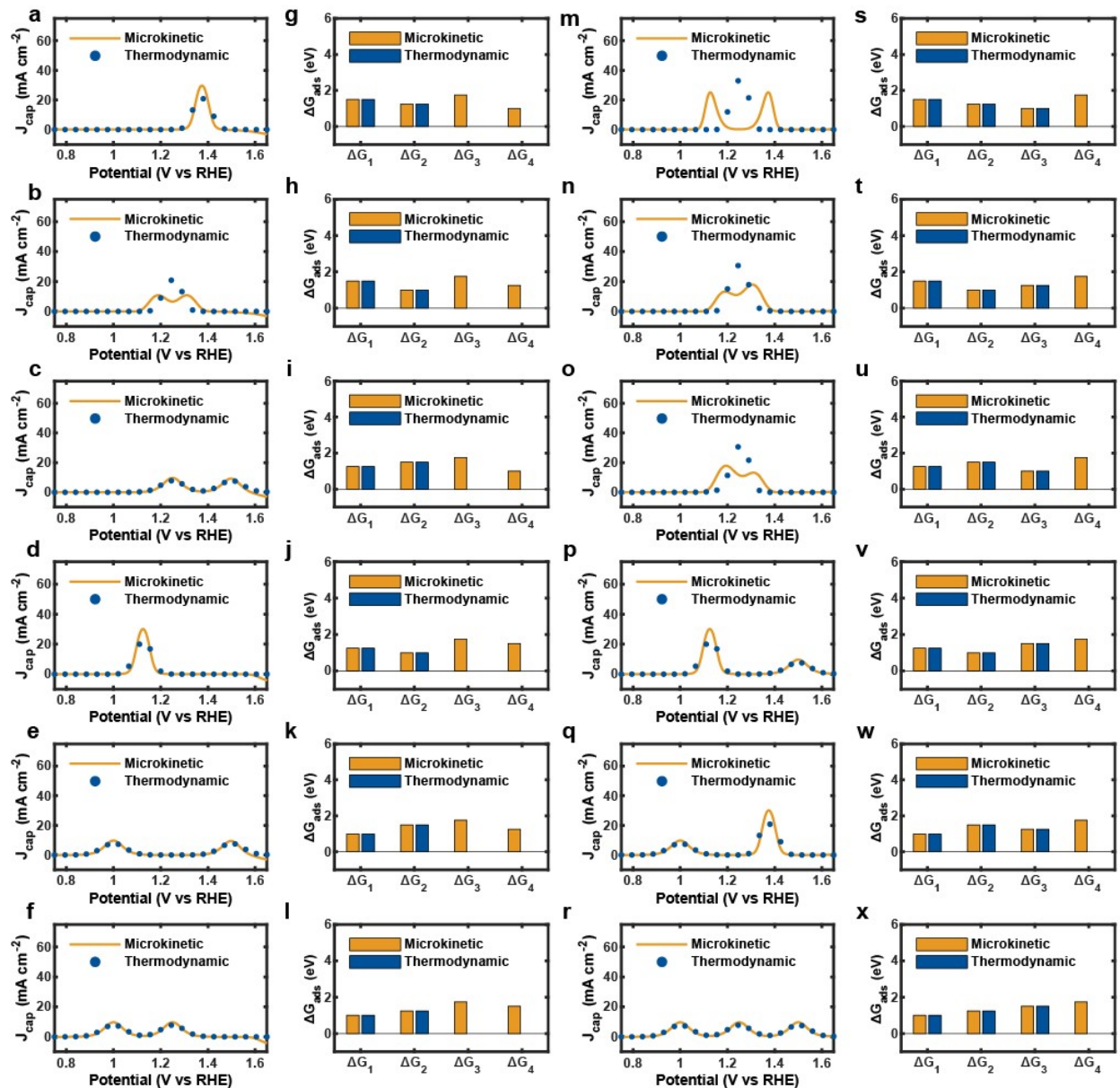
**Supplementary Fig. 11.** Summary of simulated microkinetic model with equation S10 being the rate-determining step. (a-f) Summary of the simulated  $\Delta G$  with different permutations. (g-l) Simulated CVs for different permutations of  $\Delta G$  from a to f. (m-r) Simulated electroadsorption current-voltage profiles of different permutations of  $\Delta G$  from a to f. (s-x) Simulated charge-potential profiles of different permutations of  $\Delta G$  from a to f.



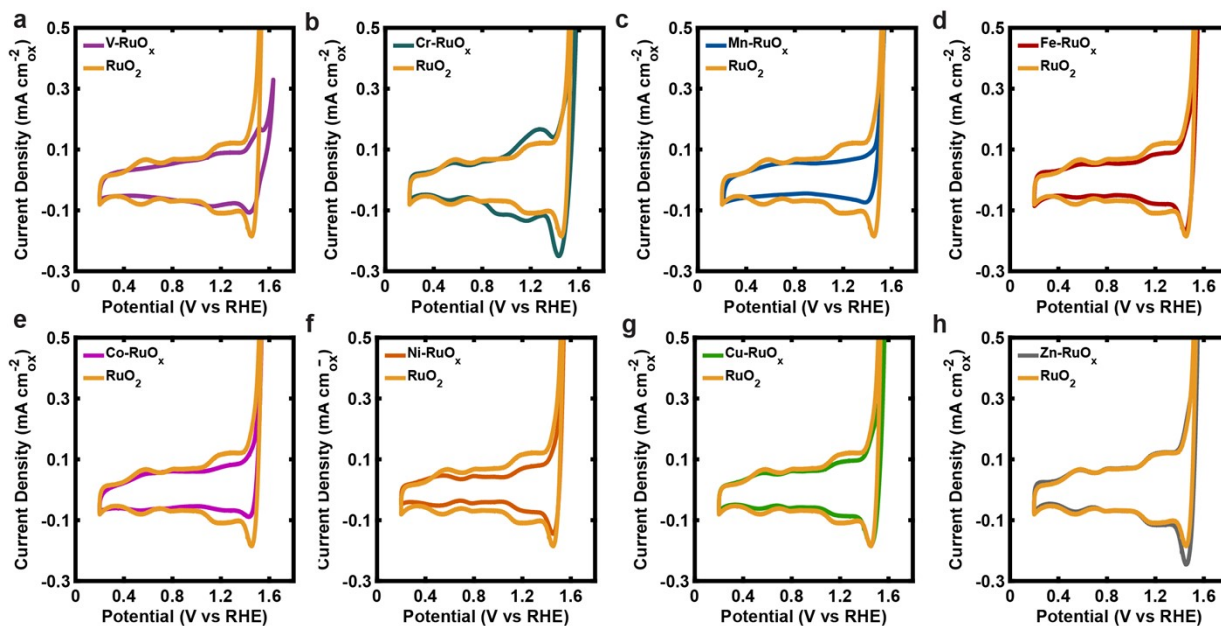
**Supplementary Fig. 12.** Summary of simulated microkinetic model with equation S11 being the rate-determining step. (a-f) Summary of the simulated  $\Delta G$  with different permutations. (g-l) Simulated CVs for different permutations of  $\Delta G$  from a to f. (m-r) Simulated electroadsorption current-voltage profiles of different permutations of  $\Delta G$  from a to f. (s-x) Simulated charge-potential profiles of different permutations of  $\Delta G$  from a to f.



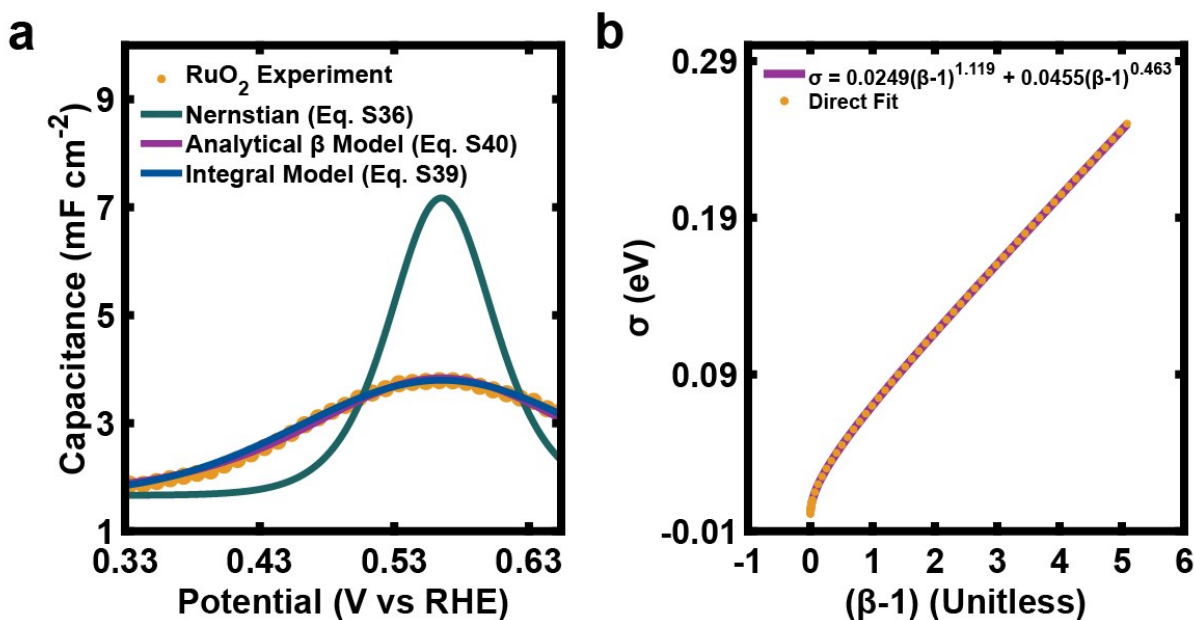
**Supplementary Fig. 13.** Summary of thermodynamic and microkinetic simulations. Simulated thermodynamic and microkinetic electroadsorption current-voltage profiles of rate-determining step being (a-f) equation S8 with  $\Delta G$  from (g-l) and (m-r) equation S9 with  $\Delta G$  from (s-x).



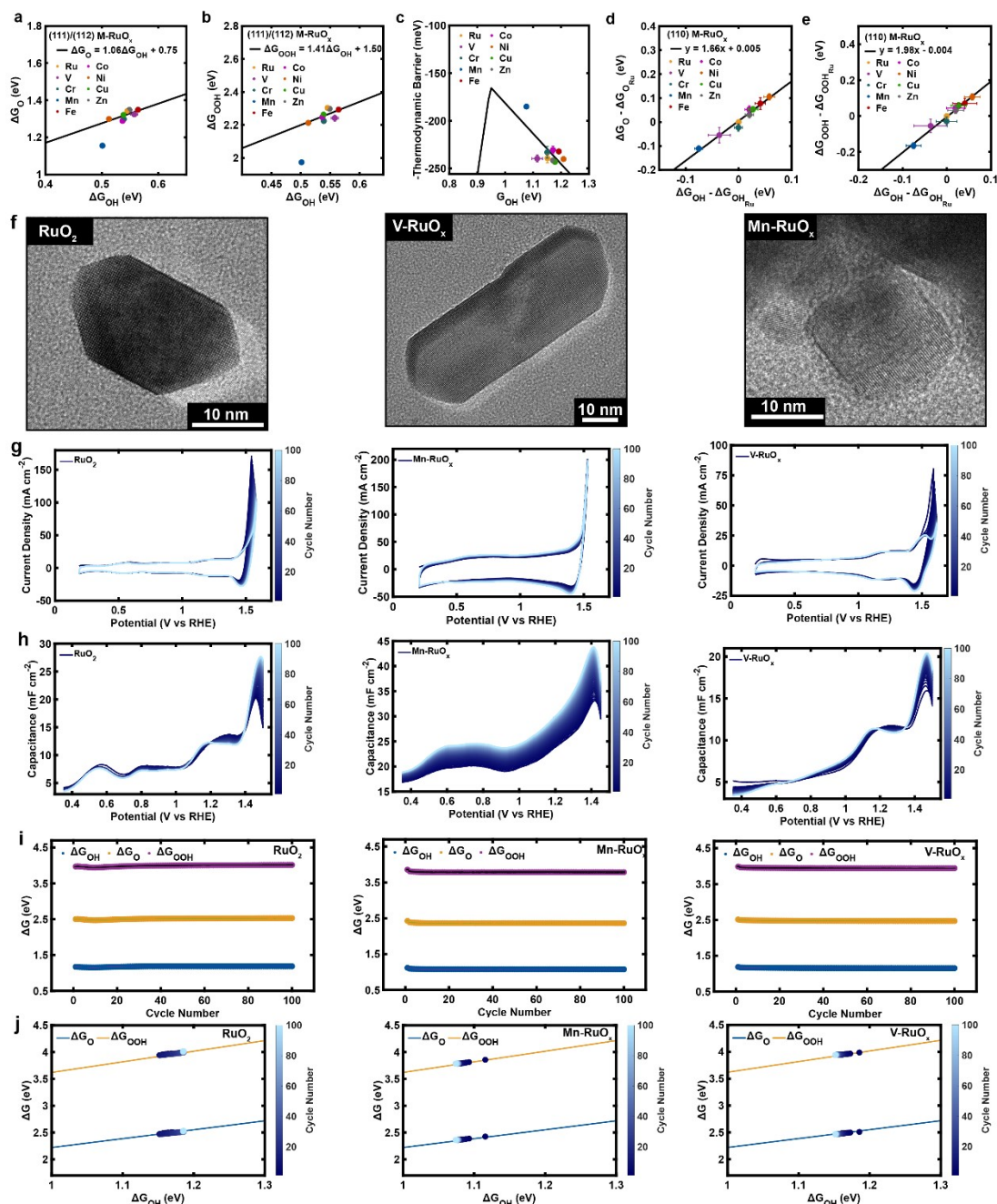
**Supplementary Fig. 14.** Summary of thermodynamic and microkinetic simulations. Simulated thermodynamic and microkinetic electroadsorption current-voltage profiles of rate-determining step being (a-f) equation S10 with  $\Delta G$  from (g-l) and (m-r) equation S11 with  $\Delta G$  from (s-x).



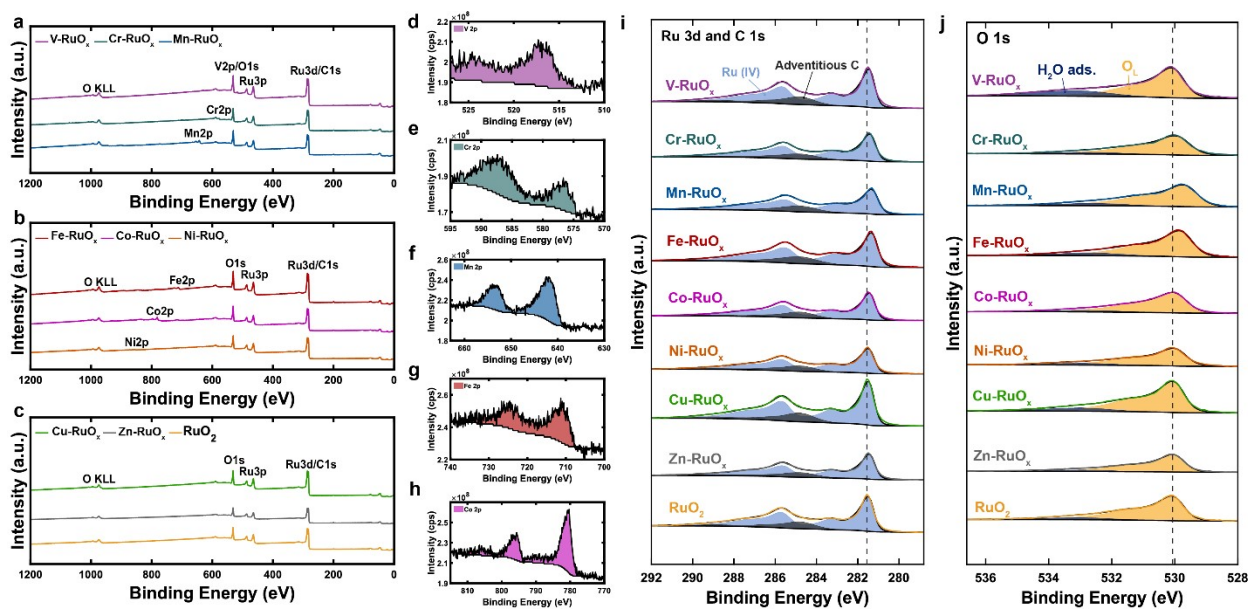
**Supplementary Fig. 15.** ECSA-corrected CVs collected at  $1000 \text{ mV s}^{-1}$  scan rate of  $\text{RuO}_2$  and  $\text{M-RuO}_x$  electrocatalysts synthesized at  $700^\circ\text{C}$ . CV of  $\text{RuO}_2$  plotted with that of (a)  $\text{V-RuO}_x$ , (b)  $\text{Cr-RuO}_x$ , (c)  $\text{Mn-RuO}_x$ , (d)  $\text{Fe-RuO}_x$ , (e)  $\text{Co-RuO}_x$ , (f)  $\text{Ni-RuO}_x$ , (g)  $\text{Cu-RuO}_x$ , and (h)  $\text{Zn-RuO}_x$ .



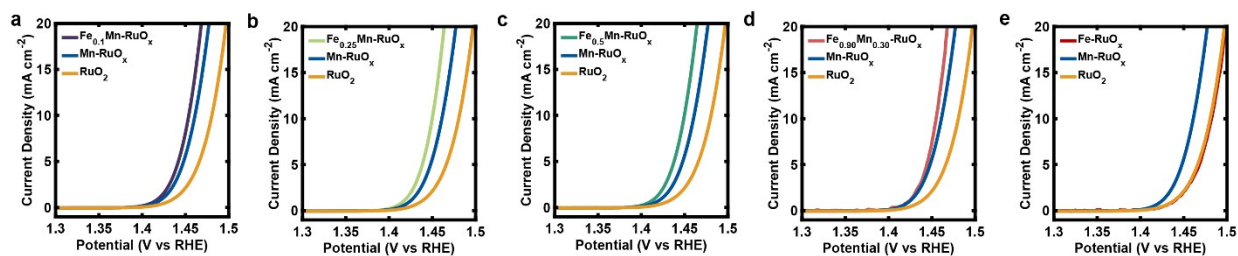
**Supplementary Fig. 16.** Peak broadening analysis of  $\text{RuO}_2$ . (a) Experimental capacitance versus potential profile for the first electroadsorption peak of  $\text{RuO}_2$  plotted with Nernstian fit, analytical  $\beta$  model fit and integral model fit. (b) Correlation between  $\sigma$  and  $\beta$ .



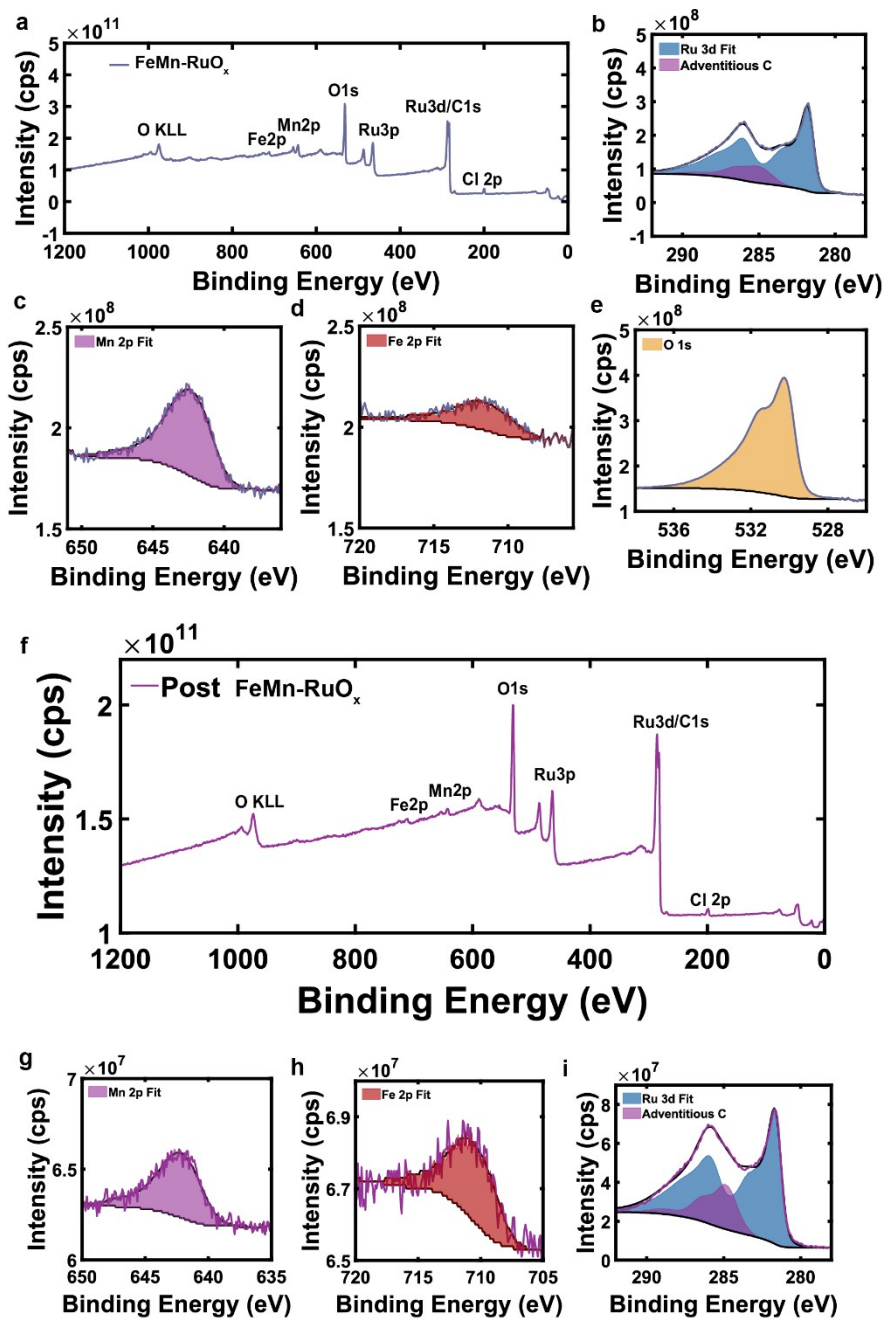
**Supplementary Fig. 17.** Summary of electroadsorption analysis for RuO<sub>2</sub> and M-RuO<sub>x</sub> synthesized at 700 °C. Experimentally derived scaling relations of (a)  $\Delta G_O$  versus  $\Delta G_{OH}$  and (b)  $\Delta G_{OOH}$  versus  $\Delta G_{OH}$  on (111)/(112) site. (c) Experimentally derived volcano plot. (d)  $\Delta G_O$  of M-RuO<sub>x</sub> -  $\Delta G_O$  of RuO<sub>2</sub> and (e)  $\Delta G_{OOH}$  of M-RuO<sub>x</sub> -  $\Delta G_{OOH}$  of RuO<sub>2</sub> versus  $\Delta G_{OH}$  of M-RuO<sub>x</sub> -  $\Delta G_{OH}$  of RuO<sub>2</sub> on the (110) site. (f) HR-TEM images of RuO<sub>2</sub> and M-RuO<sub>x</sub> nanocrystals after 100 CV cycles. (g) 100 cycles of CVs collected at 1 V s<sup>-1</sup> of RuO<sub>2</sub>, Mn-RuO<sub>x</sub> and V-RuO<sub>x</sub>. (h) Capacitance-voltage profiles of 100 cycles of CVs of RuO<sub>2</sub>, Mn-RuO<sub>x</sub> and V-RuO<sub>x</sub>. (i)  $\Delta G_{OH}$ ,  $\Delta G_O$  and  $\Delta G_{OOH}$  of (110) site for 100 cycles of CVs of RuO<sub>2</sub>, Mn-RuO<sub>x</sub> and V-RuO<sub>x</sub>. (j)  $\Delta G_O$  (blue) and  $\Delta G_{OOH}$  (orange) versus  $\Delta G_{OH}$  of (110) site for 100 cycles of CVs plotted with the scaling laws of site (110) for RuO<sub>2</sub>, Mn-RuO<sub>x</sub> and V-RuO<sub>x</sub>.



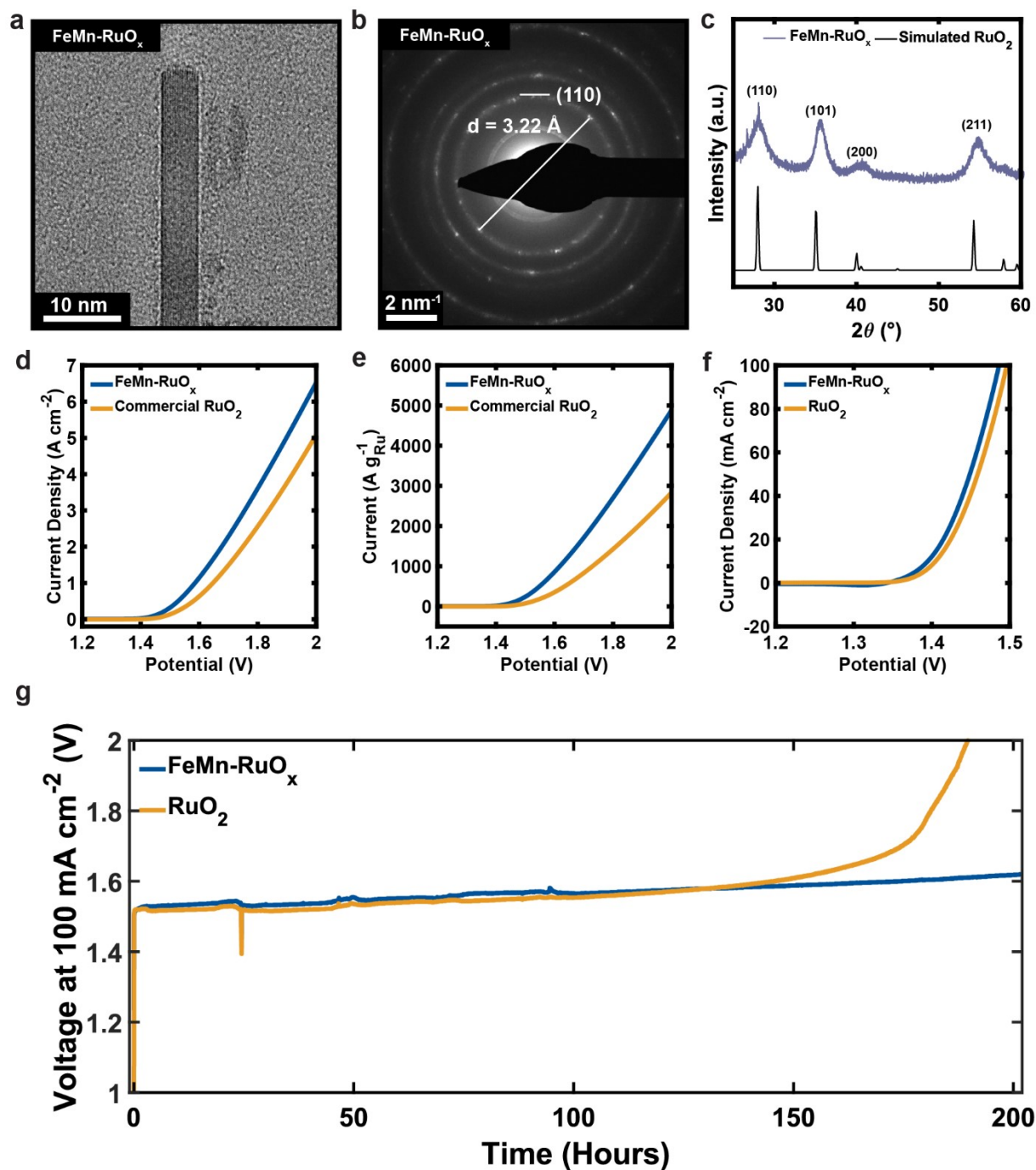
**Supplementary Fig. 18.** XPS analysis of  $\text{RuO}_2$  and  $\text{M-RuO}_x$  electrocatalysts synthesized at  $700^\circ\text{C}$ . Survey scan of (a)  $\text{V-RuO}_x$ ,  $\text{Cr-RuO}_x$ ,  $\text{Mn-RuO}_x$ , (b)  $\text{Fe-RuO}_x$ ,  $\text{Co-RuO}_x$ ,  $\text{Ni-RuO}_x$ , (c)  $\text{Cu-RuO}_x$ ,  $\text{Zn-RuO}_x$ , and  $\text{RuO}_2$ . Region scans of (d) V 2p, (e) Cr 2p, (f) Mn 2p, (g) Fe 2p, (h) Co 2p, (i) Ru 3d/C 1s, (j) O 1s.



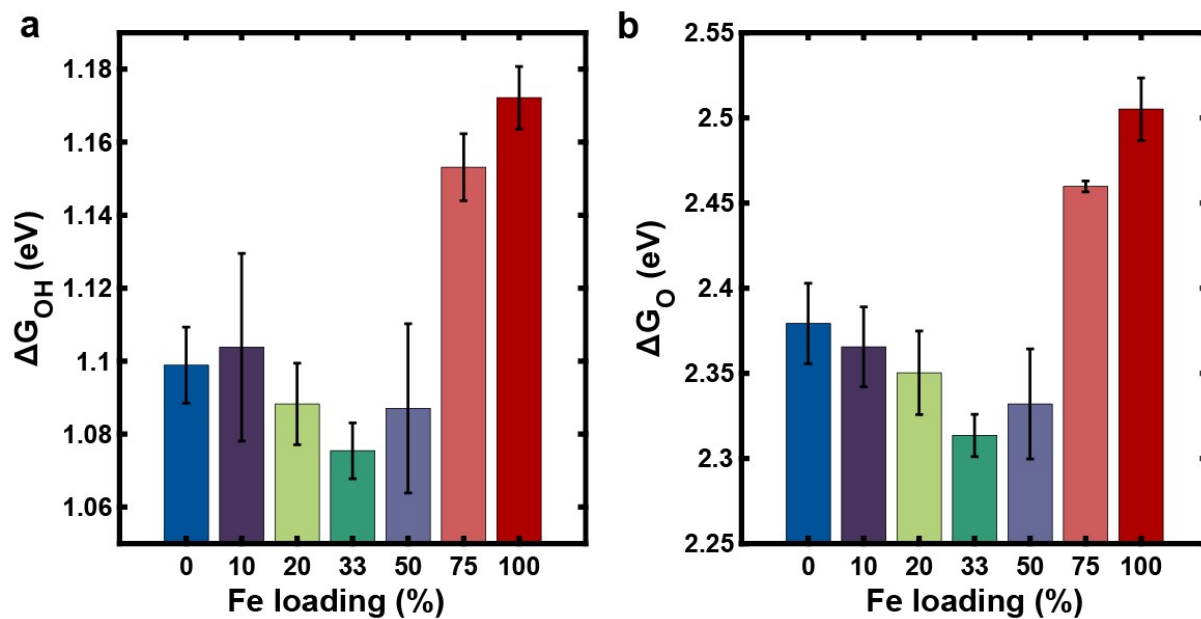
**Supplementary Fig. 19.** IR-corrected steady-state CVs collected at  $10\text{ mV s}^{-1}$  scan rate of  $\text{RuO}_2$ ,  $\text{Mn-RuO}_x$  and  $\text{FeMn-RuO}_x$  electrocatalysts with different Fe loading synthesized at  $500^\circ\text{C}$ . Plots of average IR-corrected current density versus potential of  $\text{Mn-RuO}_x$  and  $\text{RuO}_2$  plotted with that of (a)  $\text{Fe}_{0.1}\text{Mn-RuO}_x$ , (b)  $\text{Fe}_{0.25}\text{Mn-RuO}_x$ , (c)  $\text{Fe}_{0.5}\text{Mn-RuO}_x$ , (d)  $\text{Fe}_{0.90}\text{Mn}_{0.3}\text{-RuO}_x$  and (e)  $\text{Fe-RuO}_x$ .



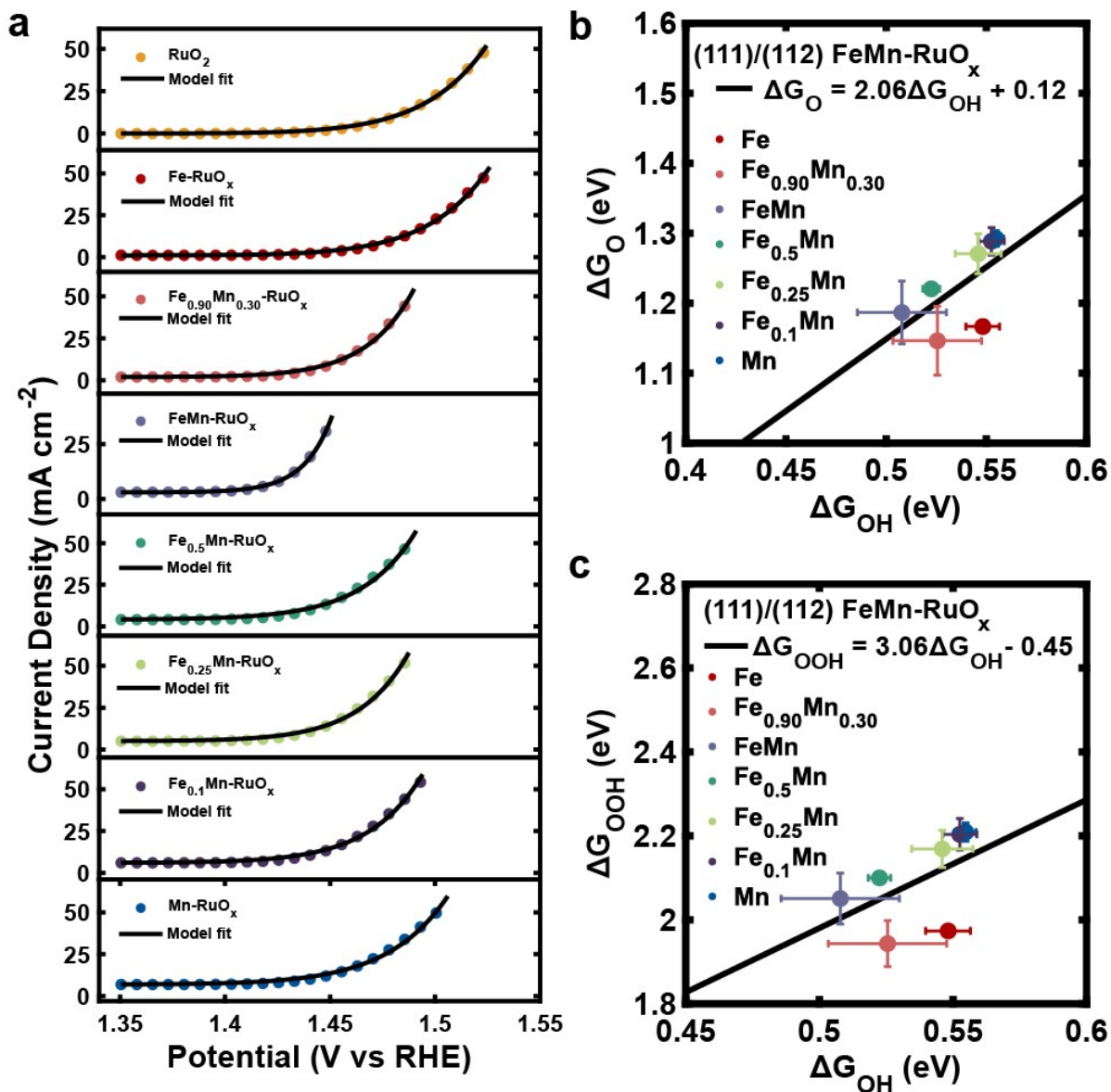
**Supplementary Fig. 20.** (a-d) XPS analysis of FeMn-RuO<sub>x</sub>. (a) Survey scan. Region scans of (b) Ru 3d/C1s, (c) Mn 2p, (d) Fe 2p, and (e) O 1s. (f-i) XPS analysis of the post OER FeMn-RuO<sub>x</sub>. (f) Survey scan. XPS region scans of (g) Mn 2p, (h) Fe 2p, and (i) Ru 3d/C 1s.



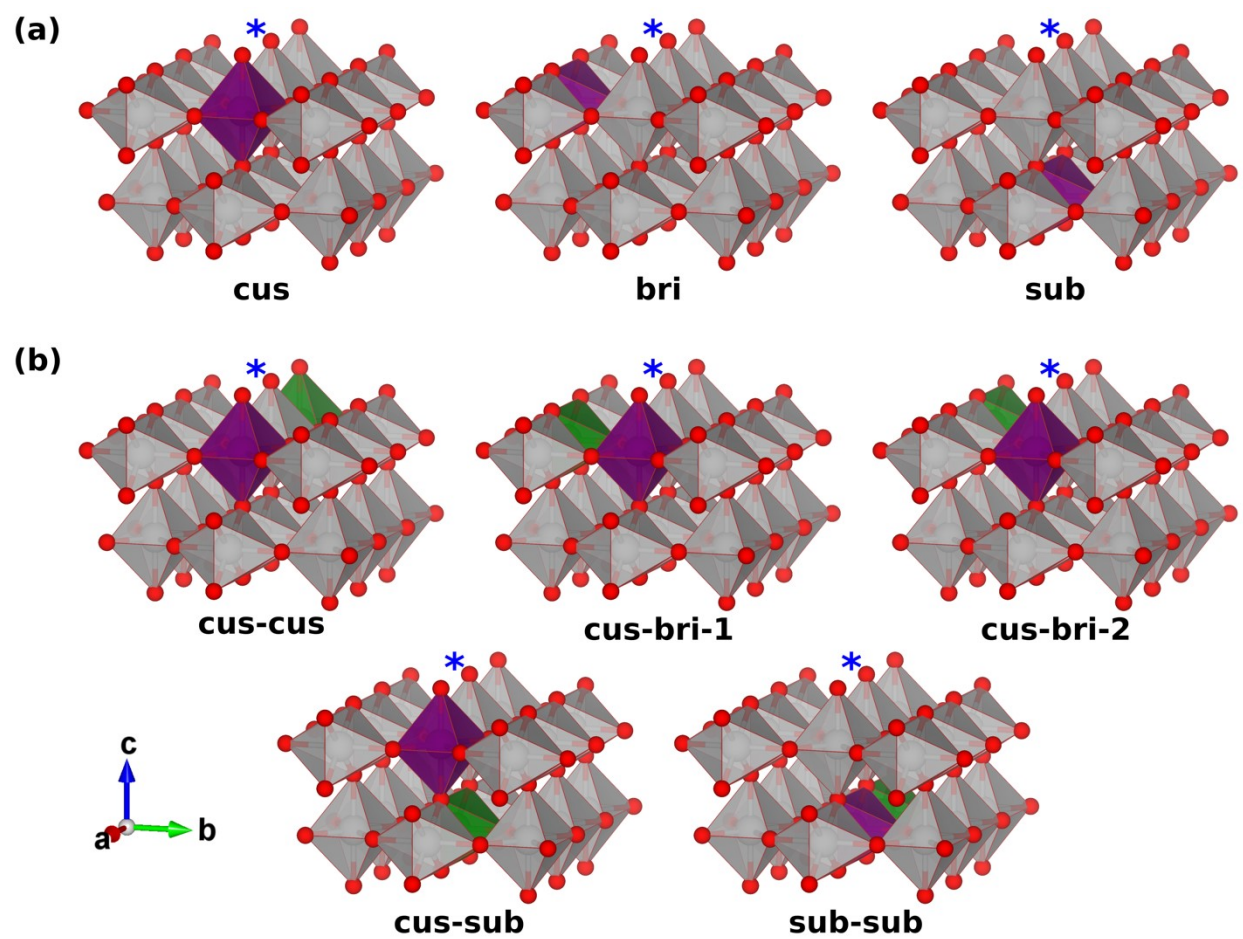
**Supplementary Fig. 21.** Characterization of FeMn-RuO<sub>x</sub> nanocrystals. (a) HR-TEM image. (b) SAED with (110) facet and d-spacing labeled. (c) Experimental XRD pattern of FeMn-RuO<sub>x</sub> and simulated XRD pattern of database RuO<sub>2</sub> with crystallographic facets labeled (ICSD-56007). Ti flow field electrolyzer activity comparison of (d) current density versus potential and (e) current per grams of Ru versus potential profiles between FeMn-RuO<sub>x</sub> synthesized at 500 °C and commercial RuO<sub>2</sub>. (f) Current-density versus potential profiles of RuO<sub>2</sub> and FeMn-RuO<sub>x</sub> synthesized at 500 °C. (g) Proton exchange membrane water electrolysis stability test of FeMn-RuO<sub>x</sub> and RuO<sub>2</sub> synthesized at 500 °C operated at 100 mA cm<sup>-2</sup>.



**Supplementary Fig. 22.** OER intermediates binding energies of FeMn-RuO<sub>x</sub> electrocatalysts with different Fe loading. (a)  $\Delta G_{\text{OH}}$  and (b)  $\Delta G_{\text{O}}$  versus percent Fe loading.



**Supplementary Fig. 23.** Summary of electroadsorption and kinetic analysis of  $\text{FeMn-RuO}_x$  with different Fe loading, M- $\text{RuO}_x$  and  $\text{RuO}_2$  synthesized at 500 °C. (a) Kinetic model fits overlap with experimentally derived catalytic current-voltage profiles. Scaling laws for (111)/(112) site of (c)  $\Delta G_{\text{O}}$  versus  $\Delta G_{\text{OH}}$  and (d)  $\Delta G_{\text{OOH}}$  versus  $\Delta G_{\text{OH}}$ .



**Supplementary Fig. 24.** Atomic structures for (a) single-site doping and (b) dual-site doping on  $\text{RuO}_2(110)$  surface. Blue asterisks denote the active site for OER. Cus, bri and sub stand for CUS, bridge and subsurface sites.

## Supplementary Tables

**Supplementary Table 1.** Summary of SEM-EDS elemental compositions of RuO<sub>2</sub>, M-RuO<sub>x</sub> synthesized at 700°C and FeMn-RuO<sub>x</sub> synthesized at 500°C on a metal basis.

Compound	Atomic % Ru	Atomic % TM	Ru:TM ratio
RuO <sub>2</sub>	100.0	0.0	1:0.00
V-RuO <sub>x</sub>	92.8	7.2	1:0.08
Cr-RuO <sub>x</sub>	82.6	17.4	1:0.21
Mn-RuO <sub>x</sub>	78.7	21.3	1:0.27
Fe-RuO <sub>x</sub>	83.3	16.7	1:0.20
Co-RuO <sub>x</sub>	47.8	52.2	1:1.09
Ni-RuO <sub>x</sub>	80.0	20.0	1:0.25
Cu-RuO <sub>x</sub>	98.0	2.0	1:0.02
Zn-RuO <sub>x</sub>	99.0	1.0	1:0.01
FeMn-RuO <sub>x</sub>	64.6	12.8 (Fe), 22.6 (Mn)	1:0.20 (Fe), 1:0.35 (Mn)
Co-RuO <sub>x</sub> as-synthesized	67.7	32.3	1:0.48
Ni-RuO <sub>x</sub> as-synthesized	46.7	53.3	1:1.14
FeMn-RuO <sub>x</sub> post	79.2	9.8 (Fe), 11.0 (Mn)	1:0.12 (Fe), 1:1.14 (Mn)

**Supplementary Table 2.** Summary of lattice parameters calculated through Rietveld refinement of RuO<sub>2</sub>, M-RuO<sub>x</sub> synthesized at 700°C and FeMn-RuO<sub>x</sub> synthesized at 500°C.

Compound	a = b	c	d-spacing (Å) (110)
RuO <sub>2</sub>	4.497(5)	3.111(3)	3.1802
V-RuO <sub>x</sub>	4.497(1)	3.1041(7)	3.1799
Cr-RuO <sub>x</sub>	4.51(2)	3.08(1)	3.1905
Mn-RuO <sub>x</sub>	4.50(2)	3.07(1)	3.1834
Fe-RuO <sub>x</sub>	4.495(6)	3.093(4)	3.1789
Cu-RuO <sub>x</sub>	4.489(2)	3.103(2)	3.1743
Zn-RuO <sub>x</sub>	4.492(2)	3.105(1)	3.1765
FeMn-RuO <sub>x</sub>	4.518(3)	3.055(9)	3.1949
Co-RuO <sub>x</sub> 1hr 2M HCl treated	4.486(6)	3.090(8)	3.1721
Co-RuO <sub>x</sub> 4hr 2M HCl treated	4.483(5)	3.089(3)	3.1703
Ni-RuO <sub>x</sub> 1hr 2M HCl treated	4.49(2)	3.11(1)	3.1763
Co-RuO <sub>x</sub> as-synthesized	4.484(6)	3.089(3)	3.1721
Ni-RuO <sub>x</sub> as-synthesized	4.494(8)	3.099(7)	3.1777

**Table 3.** Summary of overpotentials ( $\eta$ ) and mass activity of RuO<sub>2</sub>, M-RuO<sub>x</sub> synthesized at both 500°C and 700°C and FeMn-RuO<sub>x</sub> with different Fe loading synthesized at 500°C.

Compound	$\eta$ at 10 mA per cm <sup>2</sup> (mV)	$\eta$ at 0.1 mA per cm <sup>2</sup> <sub>ox</sub> (mV)	$\eta$ at 0.01 mA per cm <sup>2</sup> <sub>ox</sub> (mV)	$\eta$ at 1 s <sup>-1</sup> TOF (mV)	$\eta$ at 0.1 s <sup>-1</sup> TOF (mV)	Mass activity at 220 mV (A g <sup>-1</sup> )
<b>RuO<sub>2</sub></b>	315 ± 3	294 ± 2	242 ± 1	284 ± 3	235 ± 2	0.6 ± 0.1
<b>V-RuO<sub>x</sub></b>	389 ± 6	374 ± 6	275.9 ± 0.4	346 ± 2	257 ± 4	0.07 ± 0.01
<b>Cr-RuO<sub>x</sub></b>	313 ± 2	315 ± 1	259.8 ± 0.3	321 ± 1	264.0 ± 0.4	0.27 ± 0.02
<b>Mn-RuO<sub>x</sub></b>	239 ± 3	267 ± 4	221 ± 2	225 ± 2	197 ± 1	12 ± 2
<b>Fe-RuO<sub>x</sub></b>	308 ± 10	309 ± 4	247 ± 1	281 ± 2	236 ± 1	0.49 ± 0.05
<b>Co-RuO<sub>x</sub></b>	335 ± 5	299 ± 4	239 ± 3	260 ± 3	223 ± 2	0.35 ± 0.12
<b>Ni-RuO<sub>x</sub></b>	304 ± 3	305 ± 1	254 ± 1	283 ± 2	240 ± 2	0.41 ± 0.05
<b>Cu-RuO<sub>x</sub></b>	332 ± 2	321.4 ± 0.3	263 ± 1	312 ± 2	258 ± 1	0.09 ± 0.04
<b>Zn-RuO<sub>x</sub></b>	323 ± 3	311 ± 1	256 ± 1	309 ± 1	255 ± 1	0.21 ± 0.05
<b>RuO<sub>2</sub> 500 °C</b>	250 ± 2	276 ± 1	225.7 ± 0.4	263 ± 2	217 ± 1	9 ± 1
<b>Fe-RuO<sub>x</sub> 500 °C</b>	248 ± 5	--	243 ± 4	250 ± 4	208 ± 3	10 ± 2
<b>Fe<sub>0.90</sub>Mn<sub>0.30</sub>-RuO<sub>x</sub></b>	227 ± 2	--	228 ± 2	235.5 ± 0.7	200 ± 1	26 ± 2
<b>FeMn-RuO<sub>x</sub></b>	210 ± 6	--	210 ± 7	--	194 ± 8	84 ± 35
<b>Fe<sub>0.50</sub>Mn-RuO<sub>x</sub></b>	219 ± 2	--	214.4 ± 0.4	240 ± 5	198 ± 2	43 ± 5
<b>Fe<sub>0.25</sub>Mn-RuO<sub>x</sub></b>	221 ± 2	--	216 ± 2	235.1 ± 1	196.3 ± 0.3	37 ± 4
<b>Fe<sub>0.1</sub>Mn-RuO<sub>x</sub></b>	226 ± 1	--	214.7 ± 0.3	238.1 ± 3.6	199 ± 2	29 ± 2
<b>Mn-RuO<sub>x</sub> 500 °C</b>	233 ± 2	275.1 ± 1	218.2 ± 0.3	240 ± 2	200 ± 1	20 ± 2

**Supplementary Table 4.** Summary of measured resistances of RuO<sub>2</sub>, M-RuO<sub>x</sub> synthesized at both 500°C and 700°C and FeMn-RuO<sub>x</sub> with different Fe loading synthesized at 500°C.

<b>Compound</b>	<b>Re(Z) (Ω)</b>
<b>RuO<sub>2</sub></b>	3.4 ± 0.3
<b>V-RuO<sub>x</sub></b>	3.20 ± 0.02
<b>Cr-RuO<sub>x</sub></b>	3.4 ± 0.2
<b>Mn-RuO<sub>x</sub></b>	3.17 ± 0.05
<b>Fe-RuO<sub>x</sub></b>	3.1 ± 0.1
<b>Co-RuO<sub>x</sub></b>	3.6 ± 0.5
<b>Ni-RuO<sub>x</sub></b>	3.3 ± 0.1
<b>Cu-RuO<sub>x</sub></b>	3.3 ± 0.2
<b>Zn-RuO<sub>x</sub></b>	3.24 ± 0.04
<b>RuO<sub>2</sub> 500 °C</b>	3.30 ± 0.04
<b>Fe-RuO<sub>x</sub> 500 °C</b>	3.5 ± 0.1
<b>Fe<sub>0.90</sub> Mn<sub>0.30</sub>-RuO<sub>x</sub></b>	3.55 ± 0.07
<b>FeMn-RuO<sub>x</sub></b>	6.5 ± 0.4
<b>Fe<sub>0.50</sub> Mn-RuO<sub>x</sub></b>	3.5 ± 0.1
<b>Fe<sub>0.25</sub> Mn-RuO<sub>x</sub></b>	3.40 ± 0.05
<b>Fe<sub>0.1</sub> Mn-RuO<sub>x</sub></b>	3.46 ± 0.05
<b>Mn-RuO<sub>x</sub> 500 °C</b>	3.5 ± 0.1
<b>Commercial Co<sub>3</sub>O<sub>4</sub></b>	3.5 ± 0.2
<b>Commercial NiO</b>	3.35 ± 0.02
<b>Co-RuO<sub>x</sub> 4 hr 2M HCl treated</b>	4 ± 0.5
<b>Co-RuO<sub>x</sub> as-synthesized</b>	3.5 ± 0.2
<b>Ni-RuO<sub>x</sub> as-synthesized</b>	3.36 ± 0.09

**Supplementary Table 5.** Summary of roughness factor and site density of RuO<sub>2</sub>, M-RuO<sub>x</sub> synthesized at both 700 °C and 500 °C and FeMn-RuO<sub>x</sub> synthesized at 500 °C.

Compound	Roughness Factor	Site density (sites nm <sup>-2</sup> )
<b>RuO<sub>2</sub></b>	52 ± 8	1.68 ± 0.06
<b>V-RuO<sub>x</sub></b>	69 ± 1	0.9 ± 0.1
<b>Cr-RuO<sub>x</sub></b>	107 ± 6	2.361 ± 0.003
<b>Mn-RuO<sub>x</sub></b>	316 ± 14	0.318 ± 0.002
<b>Fe-RuO<sub>x</sub></b>	105 ± 16	0.96 ± 0.01
<b>Co-RuO<sub>x</sub></b>	39 ± 5	0.815 ± 0.002
<b>Ni-RuO<sub>x</sub></b>	102 ± 6	1.01 ± 0.06
<b>Cu-RuO<sub>x</sub></b>	72 ± 4	1.61 ± 0.07
<b>Zn-RuO<sub>x</sub></b>	69 ± 6	2.03 ± 0.06
<b>RuO<sub>2</sub> 500°C</b>	296 ± 20	1.44 ± 0.05
<b>Fe-RuO<sub>x</sub> 500 °C</b>	537 ± 28	0.29 ± 0.01
<b>Fe<sub>0.90</sub>Mn<sub>0.30</sub>-RuO<sub>x</sub></b>	1082 ± 6	0.34 ± 0.05
<b>FeMn-RuO<sub>x</sub></b>	993 ± 177	0.67 ± 0.09
<b>Fe<sub>0.50</sub>Mn-RuO<sub>x</sub></b>	778 ± 98	0.8 ± 0.1
<b>Fe<sub>0.25</sub>Mn-RuO<sub>x</sub></b>	729 ± 16	0.71 ± 0.02
<b>Fe<sub>0.1</sub>Mn-RuO<sub>x</sub></b>	537 ± 28	0.9 ± 0.1
<b>Mn-RuO<sub>x</sub> 500°C</b>	462 ± 41	0.80 ± 0.05

**Supplementary Table 6.** Summary of electroadsorption energies of RuO<sub>2</sub>, M-RuO<sub>x</sub> synthesized at both 700 °C and 500 °C and FeMn-RuO<sub>x</sub> with different Fe loading synthesized at 500 °C on (111)/(112) site.

Compound	ΔG <sub>1</sub> (eV)	ΔG <sub>2</sub> (eV)	ΔG <sub>3</sub> (eV)	Thermodynamic barrier (eV)
<b>RuO<sub>2</sub></b>	0.545 ± 0.003	0.797 ± 0.003	0.962 ± 0.003	1.38 ± 0.01
<b>V-RuO<sub>x</sub></b>	0.558 ± 0.006	0.766 ± 0.006	0.918 ± 0.008	1.45 ± 0.02
<b>Cr-RuO<sub>x</sub></b>	0.539 ± 0.002	0.759 ± 0.003	0.926 ± 0.003	1.46 ± 0.01
<b>Mn-RuO<sub>x</sub></b>	0.501 ± 0.002	0.654 ± 0.002	0.819 ± 0.001	1.713 ± 0.005
<b>Fe-RuO<sub>x</sub></b>	0.564 ± 0.001	0.784 ± 0.001	0.945 ± 0.002	1.394 ± 0.004
<b>Co-RuO<sub>x</sub></b>	0.537 ± 0.002	0.752 ± 0.001	0.958 ± 0.002	1.440 ± 0.004
<b>Ni-RuO<sub>x</sub></b>	0.513 ± 0.001	0.786 ± 0.001	0.914 ± 0.001	1.474 ± 0.001
<b>Cu-RuO<sub>x</sub></b>	0.539 ± 0.001	0.783 ± 0.002	0.942 ± 0.004	1.424 ± 0.004
<b>Zn-RuO<sub>x</sub></b>	0.5489 ± 0.0001	0.7990 ± 0.0001	0.950 ± 0.002	1.389 ± 0.002
<b>RuO<sub>2</sub> 500°C</b>	0.566 ± 0.001	0.798 ± 0.001	0.964 ± 0.002	1.359 ± 0.002
<b>Fe-RuO<sub>x</sub> 500 °C</b>	0.55 ± 0.01	0.62 ± 0.01	0.807 ± 0.004	1.71 ± 0.01
<b>Fe<sub>0.90</sub>Mn<sub>0.30</sub>-RuO<sub>x</sub></b>	0.53 ± 0.02	0.62 ± 0.03	0.80 ± 0.01	1.74 ± 0.05
<b>FeMn-RuO<sub>x</sub></b>	0.51 ± 0.02	0.68 ± 0.02	0.86 ± 0.02	1.64 ± 0.06
<b>Fe<sub>0.50</sub>Mn-RuO<sub>x</sub></b>	0.523 ± 0.004	0.698 ± 0.004	0.879 ± 0.003	1.59 ± 0.01
<b>Fe<sub>0.25</sub>Mn-RuO<sub>x</sub></b>	0.55 ± 0.01	0.72 ± 0.02	0.90 ± 0.02	1.52 ± 0.04
<b>Fe<sub>0.1</sub>Mn-RuO<sub>x</sub></b>	0.55 ± 0.01	0.74 ± 0.01	0.92 ± 0.02	1.48 ± 0.04
<b>Mn-RuO<sub>x</sub> 500°C</b>	0.555 ± 0.004	0.74 ± 0.01	0.92 ± 0.01	1.48 ± 0.02

**Supplementary Table 7.** Summary of electroadsorption energies of RuO<sub>2</sub>, M-RuO<sub>x</sub> synthesized at both 700 °C and 500 °C and FeMn-RuO<sub>x</sub> with different Fe loading synthesized at 500 °C on (110) site.

Compound	$\Delta G_1$ (eV)	$\Delta G_2$ (eV)	$\Delta G_3$ (eV)	Thermodynamic barrier (eV)
<b>RuO<sub>2</sub></b>	1.151 ± 0.007	1.313 ± 0.004	1.468 ± 0.005	0.239 ± 0.005
<b>V-RuO<sub>x</sub></b>	1.11 ± 0.02	1.29 ± 0.01	1.469 ± 0.004	0.240 ± 0.004
<b>Cr-RuO<sub>x</sub></b>	1.151 ± 0.003	1.290 ± 0.008	1.462 ± 0.006	0.233 ± 0.006
<b>Mn-RuO<sub>x</sub></b>	1.076 ± 0.002	1.277 ± 0.002	1.414 ± 0.001	0.185 ± 0.001
<b>Fe-RuO<sub>x</sub></b>	1.192 ± 0.007	1.35 ± 0.02	1.461 ± 0.001	0.231 ± 0.004
<b>Co-RuO<sub>x</sub></b>	1.171 ± 0.003	1.346 ± 0.006	1.460 ± 0.004	0.231 ± 0.004
<b>Ni-RuO<sub>x</sub></b>	1.209 ± 0.007	1.361 ± 0.001	1.469 ± 0.001	0.240 ± 0.001
<b>Cu-RuO<sub>x</sub></b>	1.178 ± 0.006	1.34 ± 0.01	1.472 ± 0.002	0.243 ± 0.002
<b>Zn-RuO<sub>x</sub></b>	1.172 ± 0.003	1.323 ± 0.003	1.471 ± 0.002	0.242 ± 0.002
<b>RuO<sub>2</sub> 500°C</b>	1.145 ± 0.004	1.312 ± 0.001	1.440 ± 0.001	0.211 ± 0.001
<b>Fe-RuO<sub>x</sub> 500 °C</b>	1.172 ± 0.009	1.33 ± 0.01	1.431 ± 0.005	0.202 ± 0.005
<b>Fe<sub>0.90</sub>Mn<sub>0.30</sub>-RuO<sub>x</sub></b>	1.153 ± 0.009	1.307 ± 0.009	1.405 ± 0.002	0.176 ± 0.002
<b>FeMn-RuO<sub>x</sub></b>	1.09 ± 0.02	1.245 ± 0.009	1.385 ± 0.009	0.160 ± 0.009
<b>Fe<sub>0.50</sub>Mn-RuO<sub>x</sub></b>	1.075 ± 0.008	1.238 ± 0.006	1.387 ± 0.002	0.158 ± 0.002
<b>Fe<sub>0.25</sub>Mn-RuO<sub>x</sub></b>	1.09 ± 0.01	1.26 ± 0.01	1.401 ± 0.005	0.172 ± 0.005
<b>Fe<sub>0.1</sub>Mn-RuO<sub>x</sub></b>	1.10 ± 0.03	1.262 ± 0.003	1.406 ± 0.005	0.177 ± 0.005
<b>Mn-RuO<sub>x</sub> 500°C</b>	1.10 ± 0.01	1.28 ± 0.01	1.414 ± 0.005	0.185 ± 0.005

**Supplementary Table 8.** Summary of heterogeneity parameters of of RuO<sub>2</sub>, M-RuO<sub>x</sub> synthesized at both 700 °C and 500 °C and FeMn-RuO<sub>x</sub> with different Fe loading synthesized at 500 °C on (111)/(112) site.

Compound	$\beta_1$	$\beta_2$	$\beta_3$
<b>RuO<sub>2</sub></b>	2.21 ± 0.06	2.40 ± 0.08	2.03 ± 0.07
<b>V-RuO<sub>x</sub></b>	3.00 ± 0.00	2.61 ± 0.05	2.36 ± 0.06
<b>Cr-RuO<sub>x</sub></b>	2.27 ± 0.05	2.01 ± 0.08	2.38 ± 0.03
<b>Mn-RuO<sub>x</sub></b>	3.00 ± 0.00	3.00 ± 0.00	3.00 ± 0.00
<b>Fe-RuO<sub>x</sub></b>	2.2 ± 0.1	2.00 ± 0.1	1.5 ± 0.1
<b>Co-RuO<sub>x</sub></b>	2.51 ± 0.02	3.00 ± 0.00	2.76 ± 0.07
<b>Ni-RuO<sub>x</sub></b>	2.36 ± 0.03	1.12 ± 0.03	1.77 ± 0.07
<b>Cu-RuO<sub>x</sub></b>	2.40 ± 0.01	2.1 ± 0.1	1.94 ± 0.03
<b>Zn-RuO<sub>x</sub></b>	2.28 ± 0.02	2.16 ± 0.03	1.73 ± 0.06
<b>RuO<sub>2</sub> 500°C</b>	2.09 ± 0.01	3.00 ± 0.00	2.60 ± 0.01
<b>Fe-RuO<sub>x</sub> 500 °C</b>	2.8 ± 0.3	2.9 ± 0.2	1.6 ± 0.1
<b>Fe<sub>0.90</sub>Mn<sub>0.30</sub>-RuO<sub>x</sub></b>	2.96 ± 0.07	2.95 ± 0.08	2.5 ± 0.1
<b>FeMn-RuO<sub>x</sub></b>	2.8 ± 0.2	3.00 ± 0.00	3.00 ± 0.00
<b>Fe<sub>0.50</sub>Mn-RuO<sub>x</sub></b>	2.79 ± 0.05	3.00 ± 0.00	3.00 ± 0.00
<b>Fe<sub>0.25</sub>Mn-RuO<sub>x</sub></b>	2.89 ± 0.05	3.00 ± 0.00	3.00 ± 0.00
<b>Fe<sub>0.1</sub>Mn-RuO<sub>x</sub></b>	2.84 ± 0.09	3.00 ± 0.00	3.00 ± 0.00
<b>Mn-RuO<sub>x</sub> 500°C</b>	2.82 ± 0.02	3.00 ± 0.00	3.00 ± 0.00

**Supplementary Table 9.** Summary of heterogeneity parameters of of RuO<sub>2</sub>, M-RuO<sub>x</sub> synthesized at both 700 °C and 500 °C and FeMn-RuO<sub>x</sub> with different Fe loading synthesized at 500 °C on (110) site.

Compound	$\beta_1$	$\beta_2$	$\beta_3$
<b>RuO<sub>2</sub></b>	2.35 ± 0.02	2.3 ± 0.2	1.42 ± 0.02
<b>V-RuO<sub>x</sub></b>	3.00 ± 0.00	2.6 ± 0.6	1.85 ± 0.02
<b>Cr-RuO<sub>x</sub></b>	2.96 ± 0.04	1.74 ± 0.06	1.9 ± 0.2
<b>Mn-RuO<sub>x</sub></b>	3.00 ± 0.00	2.59 ± 0.01	1.69 ± 0.03
<b>Fe-RuO<sub>x</sub></b>	3.00 ± 0.00	1.8 ± 0.08	1.44 ± 0.04
<b>Co-RuO<sub>x</sub></b>	3.00 ± 0.00	3.00 ± 0.00	1.46 ± 0.03
<b>Ni-RuO<sub>x</sub></b>	2.40 ± 0.08	2.0 ± 0.3	1.33 ± 0.04
<b>Cu-RuO<sub>x</sub></b>	3.00 ± 0.00	1.9 ± 0.2	1.60 ± 0.04
<b>Zn-RuO<sub>x</sub></b>	2.67 ± 0.06	1.8 ± 0.1	1.55 ± 0.02
<b>RuO<sub>2</sub> 500°C</b>	2.74 ± 0.02	2.9 ± 0.2	1.53 ± 0.04
<b>Fe-RuO<sub>x</sub> 500 °C</b>	2.5 ± 0.1	2.5 ± 0.1	1.7 ± 0.2
<b>Fe<sub>0.90</sub>Mn<sub>0.30</sub>-RuO<sub>x</sub></b>	2.88 ± 0.04	2.5 ± 0.3	1.71 ± 0.07
<b>FeMn-RuO<sub>x</sub></b>	3.00 ± 0.00	2.5 ± 0.2	2.27 ± 0.08
<b>Fe<sub>0.50</sub>Mn-RuO<sub>x</sub></b>	3.00 ± 0.00	2.6 ± 0.1	2.3 ± 0.1
<b>Fe<sub>0.25</sub>Mn-RuO<sub>x</sub></b>	3.00 ± 0.00	2.81 ± 0.05	2.1 ± 0.2
<b>Fe<sub>0.1</sub>Mn-RuO<sub>x</sub></b>	3.00 ± 0.00	2.5 ± 0.5	2.1 ± 0.2
<b>Mn-RuO<sub>x</sub> 500°C</b>	3.00 ± 0.00	2.85 ± 0.03	1.8 ± 0.2

**Supplementary Table 10.** Summary of surface coverage of of RuO<sub>2</sub>, M-RuO<sub>x</sub> synthesized at both 700 °C and 500 °C and FeMn-RuO<sub>x</sub> with different Fe loading synthesized at 500 °C on (111)/(112) site.

Compound	S* <sub>OH</sub> (mC per cm <sup>2</sup> )	S* <sub>O</sub> (mC per cm <sup>2</sup> )	S* <sub>OOH</sub> (mC per cm <sup>2</sup> )
<b>RuO<sub>2</sub></b>	0.52 ± 0.07	0.45 ± 0.09	0.26 ± 0.03
<b>V-RuO<sub>x</sub></b>	0.18 ± 0.01	0.27 ± 0.1	0.27 ± 0.01
<b>Cr-RuO<sub>x</sub></b>	0.74 ± 0.05	0.41 ± 0.01	1.1 ± 0.1
<b>Mn-RuO<sub>x</sub></b>	0.53 ± 0.03	0.65 ± 0.03	0.78 ± 0.04
<b>Fe-RuO<sub>x</sub></b>	0.34 ± 0.03	0.27 ± 0.02	0.093 ± 0.003
<b>Co-RuO<sub>x</sub></b>	0.22 ± 0.03	0.27 ± 0.04	0.16 ± 0.01
<b>Ni-RuO<sub>x</sub></b>	0.56 ± 0.03	0.16 ± 0.01	0.21 ± 0.02
<b>Cu-RuO<sub>x</sub></b>	0.52 ± 0.03	0.42 ± 0.06	0.26 ± 0.02
<b>Zn-RuO<sub>x</sub></b>	0.63 ± 0.06	0.54 ± 0.06	0.28 ± 0.04
<b>RuO<sub>2</sub> 500°C</b>	2.4 ± 0.1	2.7 ± 0.2	1.2 ± 0.1
<b>Fe-RuO<sub>x</sub> 500 °C</b>	0.9 ± 0.2	1.4 ± 0.3	0.2 ± 0.1
<b>Fe<sub>0.90</sub>Mn<sub>0.30</sub>-RuO<sub>x</sub></b>	1.8 ± 0.5	1.9 ± 0.5	1.0 ± 0.2
<b>FeMn-RuO<sub>x</sub></b>	4 ± 1	4.7 ± 0.5	4.0 ± 0.3
<b>Fe<sub>0.50</sub>Mn-RuO<sub>x</sub></b>	3.3 ± 0.2	4.3 ± 0.2	4.0 ± 0.5
<b>Fe<sub>0.25</sub>Mn-RuO<sub>x</sub></b>	3.3 ± 0.2	3.4 ± 0.3	2.9 ± 0.5
<b>Fe<sub>0.1</sub>Mn-RuO<sub>x</sub></b>	2.8 ± 0.4	3.1 ± 0.2	2.5 ± 0.2
<b>Mn-RuO<sub>x</sub> 500°C</b>	2.4 ± 0.1	2.7 ± 0.1	2.2 ± 0.2

**Supplementary Table 11.** Summary of surface coverage of of RuO<sub>2</sub>, M-RuO<sub>x</sub> synthesized at both 700 °C and 500 °C and FeMn-RuO<sub>x</sub> with different Fe loading synthesized at 500 °C on (110) site.

Compound	S* <sub>OH</sub> (mC per cm <sup>2</sup> )	S* <sub>O</sub> (mC per cm <sup>2</sup> )	S* <sub>OOH</sub> (mC per cm <sup>2</sup> )
<b>RuO<sub>2</sub></b>	0.9 ± 0.1	0.9 ± 0.2	1.2 ± 0.2
<b>V-RuO<sub>x</sub></b>	0.8 ± 0.1	0.6 ± 0.2	1.1 ± 0.2
<b>Cr-RuO<sub>x</sub></b>	3.3 ± 0.2	0.82 ± 0.04	4.9 ± 0.3
<b>Mn-RuO<sub>x</sub></b>	1.08 ± 0.05	1.63 ± 0.08	1.63 ± 0.08
<b>Fe-RuO<sub>x</sub></b>	1.3 ± 0.2	0.34 ± 0.08	1.9 ± 0.3
<b>Co-RuO<sub>x</sub></b>	0.29 ± 0.04	0.36 ± 0.06	0.35 ± 0.05
<b>Ni-RuO<sub>x</sub></b>	1.09 ± 0.08	0.7 ± 0.2	1.6 ± 0.1
<b>Cu-RuO<sub>x</sub></b>	1.3 ± 0.1	0.4 ± 0.1	2.0 ± 0.1
<b>Zn-RuO<sub>x</sub></b>	1.62 ± 0.09	0.7 ± 0.2	2.4 ± 0.1
<b>RuO<sub>2</sub> 500°C</b>	4.4 ± 0.3	5.6 ± 0.7	4.9 ± 0.3
<b>Fe-RuO<sub>x</sub> 500 °C</b>	2.8 ± 0.3	4.1 ± 0.5	4.1 ± 0.5
<b>Fe<sub>0.90</sub>Mn<sub>0.30</sub>-RuO<sub>x</sub></b>	4.1 ± 0.4	5 ± 1	5 ± 1
<b>FeMn-RuO<sub>x</sub></b>	7 ± 1	7 ± 2	10 ± 2
<b>Fe<sub>0.50</sub>Mn-RuO<sub>x</sub></b>	6.5 ± 0.5	7.3 ± 0.9	9.8 ± 0.7
<b>Fe<sub>0.25</sub>Mn-RuO<sub>x</sub></b>	4.9 ± 0.4	7.1 ± 0.4	7 ± 1
<b>Fe<sub>0.1</sub>Mn-RuO<sub>x</sub></b>	4.6 ± 0.9	4 ± 2	7 ± 2
<b>Mn-RuO<sub>x</sub> 500°C</b>	3.5 ± 0.1	5.3 ± 0.2	3.7 ± 0.9

**Supplementary Table 12.** Summary of kinetic analysis of of RuO<sub>2</sub>, M-RuO<sub>x</sub> synthesized at both 700 °C and 500 °C and FeMn-RuO<sub>x</sub> with different Fe loading synthesized at 500 °C.

Compound	E <sub>rds</sub> (eV)	$\alpha$
<b>RuO<sub>2</sub></b>	1.85 ± 0.02	0.58 ± 0.02
<b>V-RuO<sub>x</sub></b>	1.92 ± 0.02	0.59 ± 0.02
<b>Cr-RuO<sub>x</sub></b>	1.82 ± 0.03	0.75 ± 0.03
<b>Mn-RuO<sub>x</sub></b>	1.68 ± 0.02	0.89 ± 0.02
<b>Fe-RuO<sub>x</sub></b>	1.81 ± 0.02	0.68 ± 0.02
<b>Co-RuO<sub>x</sub></b>	1.80 ± 0.02	0.66 ± 0.02
<b>Ni-RuO<sub>x</sub></b>	1.78 ± 0.01	0.75 ± 0.01
<b>Cu-RuO<sub>x</sub></b>	1.83 ± 0.01	0.69 ± 0.01
<b>Zn-RuO<sub>x</sub></b>	1.84 ± 0.01	0.65 ± 0.01
<b>RuO<sub>2</sub> 500°C</b>	1.73 ± 0.01	0.87 ± 0.01
<b>Fe-RuO<sub>x</sub> 500 °C</b>	1.72 ± 0.01	0.84 ± 0.01
<b>Fe<sub>0.90</sub>Mn<sub>0.30</sub>-RuO<sub>x</sub></b>	1.651 ± 0.003	1.094 ± 0.003
<b>FeMn-RuO<sub>x</sub></b>	1.57 ± 0.01	1.72 ± 0.01
<b>Fe<sub>0.50</sub>Mn-RuO<sub>x</sub></b>	1.68 ± 0.02	0.98 ± 0.02
<b>Fe<sub>0.25</sub>Mn-RuO<sub>x</sub></b>	1.68 ± 0.02	0.97 ± 0.02
<b>Fe<sub>0.1</sub>Mn-RuO<sub>x</sub></b>	1.68 ± 0.01	0.95 ± 0.01
<b>Mn-RuO<sub>x</sub> 500°C</b>	1.72 ± 0.01	0.83 ± 0.01

**Supplementary Table 13.** Summary of XPS analysis of RuO<sub>2</sub>, M-RuO<sub>x</sub> synthesized at 700°C and FeMn-RuO<sub>x</sub> synthesized at 500°C.

Sample	Peak	Binding Energy (eV)	FWHM (eV)	Area (%)	Doublet Separation (eV)
<b>RuO<sub>2</sub></b>	Ru <sub>3d5/2</sub>	281.40	0.67	42.58	4.17
	Ru <sub>3d3/2</sub>	285.57	1.06	28.39	
	Ru <sub>3d5/2</sub> sat.	283.19	1.06	17.42	
	Ru <sub>3d3/2</sub> sat.	287.36	1.70	11.61	
	O <sub>1s</sub>	529.95	0.89	67.49	
<b>V-RuO<sub>x</sub></b>	Ru <sub>3d5/2</sub>	281.35	0.65	42.58	4.17
	Ru <sub>3d3/2</sub>	285.52	1.04	28.39	
	Ru <sub>3d5/2</sub> sat.	283.14	1.04	17.42	
	Ru <sub>3d3/2</sub> sat.	287.31	1.67	11.61	
	O <sub>1s</sub>	529.96	0.90	65.95	
<b>Cr-RuO<sub>x</sub></b>	Ru <sub>3d5/2</sub>	281.30	0.70	42.58	4.17
	Ru <sub>3d3/2</sub>	285.47	1.12	28.39	
	Ru <sub>3d5/2</sub> sat.	283.09	1.12	17.42	
	Ru <sub>3d3/2</sub> sat.	287.26	1.78	11.61	
	O <sub>1s</sub>	529.82	1.07	75.50	
<b>Mn-RuO<sub>x</sub></b>	Ru <sub>3d5/2</sub>	281.21	0.78	42.58	4.17
	Ru <sub>3d3/2</sub>	285.38	1.24	28.39	
	Ru <sub>3d5/2</sub> sat.	282.00	1.24	17.42	
	Ru <sub>3d3/2</sub> sat.	287.17	1.99	11.61	
	O <sub>1s</sub>	529.56	1.05	70.30	
<b>Fe-RuO<sub>x</sub></b>	Ru <sub>3d5/2</sub>	281.22	0.72	42.58	4.17
	Ru <sub>3d3/2</sub>	285.39	1.15	28.39	
	Ru <sub>3d5/2</sub> sat.	283.01	1.15	17.42	
	Ru <sub>3d3/2</sub> sat.	287.18	1.84	11.61	
	O <sub>1s</sub>	529.70	0.97	71.53	
<b>Co-RuO<sub>x</sub></b>	Ru <sub>3d5/2</sub>	281.33	0.66	42.58	4.17
	Ru <sub>3d3/2</sub>	285.50	1.05	28.39	
	Ru <sub>3d5/2</sub> sat.	283.12	1.05	17.42	
	Ru <sub>3d3/2</sub> sat.	287.29	1.68	11.61	
	O <sub>1s</sub>	529.89	1.03	75.68	
<b>Ni-RuO<sub>x</sub></b>	Ru <sub>3d5/2</sub>	281.38	0.70	42.58	4.17
	Ru <sub>3d3/2</sub>	285.55	1.12	28.39	
	Ru <sub>3d5/2</sub> sat.	283.17	1.12	17.42	
	Ru <sub>3d3/2</sub> sat.	287.34	1.78	11.61	
	O <sub>1s</sub>	529.89	0.94	68.88	
<b>Cu-RuO<sub>x</sub></b>	Ru <sub>3d5/2</sub>	281.38	0.66	42.58	4.17
	Ru <sub>3d3/2</sub>	285.55	1.05	28.39	
	Ru <sub>3d5/2</sub> sat.	283.17	1.05	17.42	
	Ru <sub>3d3/2</sub> sat.	287.34	1.69	11.61	
	O <sub>1s</sub>	529.93	0.87	67.54	
<b>Zn-RuO<sub>x</sub></b>	Ru <sub>3d5/2</sub>	281.34	0.66	42.58	4.17
	Ru <sub>3d3/2</sub>	285.51	1.06	28.39	
	Ru <sub>3d5/2</sub> sat.	283.13	1.06	17.42	
	Ru <sub>3d3/2</sub> sat.	287.30	1.69	11.61	
	O <sub>1s</sub>	529.92	0.87	69.64	
<b>FeMn-RuO<sub>x</sub></b>	Ru <sub>3d5/2</sub>	281.56	0.94	42.58	4.17
	Ru <sub>3d3/2</sub>	285.73	1.51	28.39	
	Ru <sub>3d5/2</sub> sat.	283.35	1.51	17.42	
	Ru <sub>3d3/2</sub> sat.	287.52	2.41	11.61	
	O <sub>1s</sub>	529.95	1.17	67.27	

**Supplementary Table 14.** DFT calculated OER energetics of M-RuO<sub>x</sub> (M = Ru, Mn, Fe) on (110) site.

<b>M-RuO<sub>x</sub> (110)</b>	<b><math>\Delta G_1</math> (eV)</b>	<b><math>\Delta G_2</math> (eV)</b>	<b><math>\Delta G_3</math> (eV)</b>	<b><math>\Delta G_4</math> (eV)</b>	<b><math>\eta</math> (eV)</b>
<b>Ru</b>	0.77	1.06	1.87	1.22	0.64
<b>Mn<sub>cus</sub></b>	0.74	1.02	2.00	1.16	0.77
<b>Mn<sub>bri</sub></b>	0.78	1.08	1.90	1.17	0.67
<b>Mn<sub>sub</sub></b>	0.69	1.10	1.85	1.28	0.62
<b>Fe<sub>cus</sub></b>	0.76	1.13	1.87	1.16	0.64
<b>Fe<sub>bri</sub></b>	0.40	1.43	1.91	1.19	0.68
<b>Fe<sub>sub</sub></b>	0.80	1.14	1.78	1.20	0.55
<b>Mn<sub>cus</sub>, Fe<sub>cus</sub></b>	0.64	1.16	1.99	1.13	0.76
<b>Mn<sub>sub</sub>, Fe<sub>sub</sub></b>	0.70	1.22	1.61	1.39	0.38
<b>Mn<sub>bri-1</sub>, Fe<sub>cus</sub></b>	0.91	0.90	2.19	0.92	0.96
<b>Mn<sub>bri-2</sub>, Fe<sub>cus</sub></b>	0.67	1.11	1.95	1.18	0.72
<b>Mn<sub>sub</sub>, Fe<sub>cus</sub></b>	0.67	1.10	1.93	1.22	0.70
<b>Mn<sub>cus</sub>, Fe<sub>bri-1</sub></b>	0.52	1.22	2.03	1.14	0.80
<b>Mn<sub>cus</sub>, Fe<sub>bri-2</sub></b>	1.05	0.73	2.19	0.94	0.96
<b>Mn<sub>cus</sub>, Fe<sub>sub</sub></b>	0.65	1.19	1.89	1.19	0.66

**Supplementary Table 15.** DFT calculated band centers of M-RuO<sub>x</sub> (M = Ru, Mn, Fe) on (110) site.

<b>M-RuO<sub>x</sub> (110)</b>	<b>*O<sub>cus</sub> 2p (eV)</b>	<b>Ru 4d (eV)</b>	<b>4d - 2p (eV)</b>
<b>Ru</b>	-2.61	-1.90	0.72
<b>Mn<sub>cus</sub></b>	-2.54	-1.72	0.82
<b>Mn<sub>bri</sub></b>	-2.57	-1.74	0.83
<b>Mn<sub>sub</sub></b>	-2.56	-1.75	0.81
<b>Fe<sub>cus</sub></b>	-2.55	-1.78	0.77
<b>Fe<sub>bri</sub></b>	-2.61	-1.84	0.78
<b>Fe<sub>sub</sub></b>	-2.59	-1.89	0.70
<b>Mn<sub>cus</sub>, Fe<sub>cus</sub></b>	-2.53	-1.77	0.76
<b>Mn<sub>sub</sub>, Fe<sub>sub</sub></b>	-2.66	-1.95	0.71
<b>Mn<sub>bri-1</sub>, Fe<sub>cus</sub></b>	-2.58	-1.75	0.84
<b>Mn<sub>bri-2</sub>, Fe<sub>cus</sub></b>	-2.58	-1.77	0.80
<b>Mn<sub>sub</sub>, Fe<sub>cus</sub></b>	-2.57	-1.79	0.78
<b>Mn<sub>cus</sub>, Fe<sub>bri-1</sub></b>	-2.61	-1.79	0.82
<b>Mn<sub>cus</sub>, Fe<sub>bri-2</sub></b>	-2.60	-1.80	0.80
<b>Mn<sub>cus</sub>, Fe<sub>sub</sub></b>	-2.60	-1.85	0.76

**Supplementary Table 16.** DFT calculated Bader charges of of M-RuO<sub>x</sub> (M = Ru, Mn, Fe) on (110) site.

<b>M-RuO<sub>x</sub> (110)</b>	<b>*O<sub>cus</sub></b>	<b>Ru</b>	<b>Mn</b>	<b>Fe</b>
<b>Ru</b>	-0.53	1.98	-	-
<b>Mn<sub>cus</sub></b>	-0.52	1.96	1.70	-
<b>Mn<sub>bri</sub></b>	-0.42	1.88	1.80	-
<b>Mn<sub>sub</sub></b>	-0.52	1.99	1.81	-
<b>Fe<sub>cus</sub></b>	-0.41	1.87	-	1.55
<b>Fe<sub>bri</sub></b>	-0.42	1.88	-	1.59
<b>Fe<sub>sub</sub></b>	-0.54	1.99	-	1.45
<b>Mn<sub>cus</sub>, Fe<sub>cus</sub></b>	-0.52	1.98	1.80	1.51
<b>Mn<sub>sub</sub>, Fe<sub>sub</sub></b>	-0.50	1.98	1.82	1.43
<b>Mn<sub>bri-1</sub>, Fe<sub>cus</sub></b>	-0.43	1.91	1.78	1.56
<b>Mn<sub>bri-2</sub>, Fe<sub>cus</sub></b>	-0.43	1.90	1.82	1.56
<b>Mn<sub>sub</sub>, Fe<sub>cus</sub></b>	-0.49	1.97	1.81	1.54
<b>Mn<sub>cus</sub>, Fe<sub>bri-1</sub></b>	-0.44	1.90	1.73	1.58
<b>Mn<sub>cus</sub>, Fe<sub>bri-2</sub></b>	-0.50	1.97	1.70	1.59
<b>Mn<sub>cus</sub>, Fe<sub>sub</sub></b>	-0.44	1.87	1.70	1.53

**Supplementary Table 17.** Summary of Rietveld analysis of Ni-RuO<sub>x</sub> and Co-RuO<sub>x</sub> samples. Surface area estimates were obtained from the weight percent, estimated particle size, and assuming the particles had a cubic morphology.

<b>Sample</b>	<b>RuO<sub>2</sub> Rel. Mass (wt %)</b>	<b>Co<sub>3</sub>O<sub>4</sub> Rel. Mass (wt %)</b>	<b>NiO Rel. Mass (wt %)</b>	<b>RuO<sub>2</sub> size (Å)</b>	<b>Co<sub>3</sub>O<sub>4</sub> size (Å)</b>	<b>NiO size (Å)</b>	<b>Co<sub>3</sub>O<sub>4</sub> Area (%)</b>	<b>NiO Area (%)</b>
<b>Ni-RuO<sub>x</sub> (0 hr)</b>	67.29	-	32.71	94.17	-	339.57	-	12.26
<b>Ni-RuO<sub>x</sub> (1 hr)</b>	91.06	-	8.94	98.50	-	65535.00	-	0.02
<b>Co-RuO<sub>x</sub> (0 hr)</b>	88.66	11.34	-	156.32	262.93	-	8.03	-
<b>Co-RuO<sub>x</sub> (1 hr)</b>	97.88	2.12	-	144.35	2137.37	-	0.34	-
<b>Co-RuO<sub>x</sub> (4 hr)</b>	96.63	3.37	-	249.90	3702.38	-	0.28	-

## **References**

- (1) Soderstedt, C. J.; Yuan, Y.; Vigil, S. A.; Ford, H. H.; Fratarcangeli, M.; Lin, Z.; Chen, J. G.; Moreno-Hernandez, I. A. Oxidized Overlayers of Ruthenium and Iridium as Electrocatalysts for Anodic Reactions. *J. Am. Chem. Soc.* **2025**. DOI: 10.1021/jacs.5c04767.
- (2) Vigil, S. A.; Moreno-Hernandez, I. A. Dissolution Heterogeneity Observed in Anisotropic Ruthenium Dioxide Nanocrystals via Liquid-Phase Transmission Electron Microscopy. *J. Am. Chem. Soc.* **2024**, *146* (16), 11133-11140. DOI: 10.1021/jacs.3c13709.
- (3) Fratarcangeli, M.; Vigil, S. A.; Lin, Z.; Soderstedt, C. J.; Moreno-Hernandez, I. A. Direct observation of structural disorder effects on iridium dioxide nanocrystal dissolution. *Matter* **2025**. DOI: 10.1016/j.matt.2024.11.003.
- (4) Song, H.; Yong, X.; Waterhouse, G. I. N.; Yu, J.; Wang, H.; Cai, J.; Tang, Z.; Yang, B.; Chang, J.; Lu, S. RuO<sub>2</sub>-CeO<sub>2</sub> Lattice Matching Strategy Enables Robust Water Oxidation Electrocatalysis in Acidic Media via Two Distinct Oxygen Evolution Mechanisms. *ACS Catal.* **2024**, *14* (5), 3298-3307. DOI: 10.1021/acscatal.3c06182.
- (5) Edgington, J.; Deberghes, A.; Seitz, L. C. Glassy Carbon Substrate Oxidation Effects on Electrode Stability for Oxygen Evolution Reaction Catalysis Stability Benchmarking. *ACS Appl. Energy Mater.* **2022**, *5* (10), 12206-12218. DOI: 10.1021/acsaem.2c01690.
- (6) Morgan, D. J. Resolving ruthenium: XPS studies of common ruthenium materials. *Surf. Interface Anal.* **2015**, *47* (11), 1072-1079. DOI: 10.1002/sia.5852.
- (7) Biesinger, M. C.; Payne, B. P.; Grosvenor, A. P.; Lau, L. W. M.; Gerson, A. R.; Smart, R. S. C. Resolving surface chemical states in XPS analysis of first row transition metals, oxides and hydroxides: Cr, Mn, Fe, Co and Ni. *Appl. Surf. Sci.* **2011**, *257* (7), 2717-2730. DOI: 10.1016/j.apsusc.2010.10.051.
- (8) McCrory, C. C. L.; Jung, S.; Peters, J. C.; Jaramillo, T. F. Benchmarking Heterogeneous Electrocatalysts for the Oxygen Evolution Reaction. *J. Am. Chem. Soc.* **2013**, *135* (45), 16977-16987. DOI: 10.1021/ja407115p.
- (9) Kuo, D.-Y.; Paik, H.; Kloppenburg, J.; Faeth, B.; Shen, K. M.; Schlom, D. G.; Hautier, G.; Suntivich, J. Measurements of Oxygen Electrodesorption Energies and Oxygen Evolution Reaction on RuO<sub>2</sub>(110): A Discussion of the Sabatier Principle and Its Role in Electrocatalysis. *J. Am. Chem. Soc.* **2018**, *140* (50), 17597-17605. DOI: 10.1021/jacs.8b09657.